remote sensing

MDPI

Article

Landslide Detection and Susceptibility Mapping by AIRSAR Data Using Support Vector Machine and Index of Entropy Models in Cameron Highlands, Malaysia

Dieu Tien Bui [1,2] **, Himan Shahabi** [3,*] **, Ataollah Shirzadi** [4] **, Kamran Chapi** [4] **, Mohsen Alizadeh** [5] **, Wei Chen** [6] **, Ayub Mohammadi** [7] **, Baharin Bin Ahmad** [7] **, Mahdi Panahi** [8] **, Haoyuan Hong** [9,10] **and Yingying Tian** [11]

[1]   Geographic Information Science Research Group, Ton Duc Thang University, Ho Chi Minh City, Vietnam; buitiendieu@tdt.edu.vn
[2]   Faculty of Environment and Labour Safety, Ton Duc Thang University, Ho Chi Minh City, Vietnam
[3]   Department of Geomorphology, Faculty of Natural Resources, University of Kurdistan, Sanandaj 66177-15175, Iran
[4]   Department of Rangeland and Watershed Management, Faculty of Natural Resources, University of Kurdistan, Sanandaj 66177-15175, Iran; A.Shirzadi@uok.ac.ir (A.S.); k.chapi@uok.ac.ir (K.C.)
[5]   Department of Urban Regional Planning, Faculty of Built Environment, Universiti Teknology Malaysia (UTM), Skudai 81310, Malaysia; alizadeh.mohsen2003@yahoo.com
[6]   College of Geology & Environment, Xi'an University of Science and Technology, Xi'an 710054, China; chenwei.0930@163.com
[7]   Department of Geoinformation, Faculty of Geoinformation and Real Estate, Universiti Teknologi Malaysia (UTM), Skudai 81310, Malaysia; ayubmohammadi1990@gmail.com (A.M.); baharinahmad@utm.my (B.B.A.)
[8]   Young Researchers and Elites Club, North Tehran Branch, Islamic Azad University, Tehran P.O. Box 19585/466, Iran; panahi2012@yahoo.com
[9]   Key Laboratory of Virtual Geographic Environment, Nanjing Normal University, Nanjing 210023, China; hong_haoyuan@outlook.com
[10]   State Key Laboratory Cultivation Base of Geographical Environment Evolution (Jiangsu Province), Nanjing 210023, China
[11]   Key Laboratory of Active Tectonics and Volcano, Institute of Geology, China Earthquake Administration, Beijing 100029, China; yingying.Tian@yahoo.com
*   Correspondence: h.shahabi@uok.ac.ir; Tel.: +98-9186658739

check for updates

Abstract: Since landslide detection using the combination of AIRSAR data and GIS-based susceptibility mapping has been rarely conducted in tropical environments, the aim of this study is to compare and validate support vector machine (SVM) and index of entropy (IOE) methods for landslide susceptibility assessment in Cameron Highlands area, Malaysia. For this purpose, ten conditioning factors and observed landslides were detected by AIRSAR data, WorldView-1 and SPOT 5 satellite images. A spatial database was generated including a total of 92 landslide locations encompassing the same number of observed and detected landslides, which was divided into training (80%; 74 landslide locations) and validation (20%; 18 landslide locations) datasets. Results of the difference between observed and detected landslides using root mean square error (RMSE) indicated that only 16.3% error exists, which is fairly acceptable. The validation process was performed using statistical-based measures and the area under the receiver operating characteristic (AUROC) curves. Results of validation process indicated that the SVM model has the highest values of sensitivity (88.9%), specificity (77.8%), accuracy (83.3%), Kappa (0.663) and AUROC (84.5%), followed by the IOE model. Overall, the SVM model applied to detected landslides is considered to

be a promising technique that could be tested and utilized for landslide susceptibility assessment in tropical environments.

1. Introduction

Natural disasters, such as landslides, floods, earthquakes, hurricanes, soil erosion and tsunamis, cause huge damages to properties and human lives, among which, landslides are known as one of the most important natural disasters worldwide [1], which are responsible for at least 17% of all natural hazard fatalities [2].

In Southeast Asia, landslides are one of the most common disasters due to its special climate condition, mountainous terrain and socioeconomic circumstances [3]. Torrential rainfalls, which cause the heavy flow of mudslides, are the main trigger of landslides and their damages in Cameron Highlands area, Malaysia [4]. Pradhan et al. (2010) reported that during 2006–2009, numerous landslides in the Cameron Highlands occurred due to torrential rainfalls, causing millions of dollars of property losses, as well as many fatal events [4]. Though few landslides occurred in residential areas, in the Cameron Highlands, many of the landslides have occurred along roads and highways due to human interference (man-made/anthropogenic factor) and triggering factors such as heavy rainfall. This means that humans have prepared the conditions for landslides' occurrence through the balance stability disturbance of natural slopes (no artificial slopes) [5]. In recent years, there have been numerous landslides and mudflow events occurring in the Cameron Highlands, resulting in enormous socio-economic damages. Landslide susceptibility, hazard and risk assessment is ineffective due to the lack of reliable landslide inventory maps. Landslide susceptibility assessment can be achieved by providing accurate landslide information and easily accessible and continuous risk data [6]. Therefore, an accurate susceptibility mapping can provide key information for a large variety of users [7]. In Cameron Highlands area in Malaysia, landslide mapping is difficult because of the dense vegetation covering landslides and the cloudy and rainy weather conditions [8]. Consequently, it is of high necessity to obtain reliable landslide susceptibility maps using accurate data and new techniques in tropical areas for purposes such as implementing landslide mitigation measures [9].

In recent years, radars have given a new dimension to doing research on disaster management with precise and real-time information [10]. Synthetic aperture radar (SAR) is an active remote sensing system, which collects data day and night, no matter under what kind of weather condition. SAR data have been applied to natural hazards' researches independently or in combination with data obtained from other remote sensing sensors [11,12]. The combination of optical and SAR data can also be used in geo-hazards' identification and susceptibility mapping and is especially popular in landslide studies [13–17]. Remote sensing is the foundation of landslide inventory maps and related thematic maps. Previous studies have demonstrated the potential of remote sensing data for the extraction of causal factors and finding landslide-prone areas [18–21].

There is no standard procedure for the production of landslide susceptibility maps [22]. Recently, because of remote sensing data together with data from other sources and the highly-developed geographic information system (GIS), the preparation of different thematic layers that are responsible for the occurrence of landslides can be accomplished in a region [23–27]. During the last few decades, the feasibility and effectiveness of using GIS and remote sensing technologies to assess landslide susceptibility modeling have been proven [28–32]. Currently, a variety of GIS-based methods are being used for landslide susceptibility modeling with less input data.

A large number of quantitative models have been proposed to integrate the causal factors and applied to landslide susceptibility mapping [33]. Recently, a variety of models have been used for landslide susceptibility mapping such as the analytical hierarchy process [34–37] and logistic

regression [38–44]. Probabilistic models have also been applied to landslide susceptibility mapping, for instance the frequency ratio [5,37,39,44–49], certainty factors [2,50–53], weight of evidence [54,55] and evidential belief function [56–58] methods.

Besides the above-mentioned methods, various data mining approaches have also been employed to map landslide susceptibility, such as neuro-fuzzy [4,59], artificial neural network [60–62], random forest [63–66], decision trees [67–69], support vector machines [62,68,70–73] and naive Bayes [74]. Hybrid methods have also been developed by combining statistical methods with data mining approaches such as the adaptive neuro-fuzzy inference system (ANFIS) and the stepwise weight assessment ratio analysis (SWARA) technique [75,76], ANN-Bayes analysis [77,78] and rough set (RS)-SVM [79,80]. Each approach depends on different logical explanations in order to generate an objective landslide susceptibility mapping and decrease the subjective evaluation of experts.

Earlier studies have shown that in the Cameron Highlands, landslide studies have been conducted in three different forms: (i) only landslide detection by remote sensing data [8,32]; (ii) landslide susceptibility mapping [4,5,40]; and (iii) landslide detection by the combination of remote sensing data and susceptibility mapping using other techniques [30]. In this case, Shahabi and Hashim (2015) detected landslides in the Cameron Highlands and prepared a landslide susceptibility map using three multi-criteria decision making models including the analytical hierarchy process (AHP), weighted linear combination (WLC) and spatial multi-criteria evaluation (SMCE) models [30]. Although some studies have been conducted on landslide assessment using detection by remote sensing data and susceptibility mapping over the different case studies individually, few studies have taken into account both landslide detection and susceptibility mapping in tropical areas such as Cameron Highlands. Therefore, the difference between the current study from earlier studies in the Cameron Highlands is the use of remote sensing data, AIRSAR (C-, L- and P-band images) and optical satellite images for landslide detection to obtain an accurate landslide inventory map, as well as the application of a machine learning algorithm, SVM, and a bivariate statistical model, the index of entropy (IOE), for landslide susceptibility mapping of the Cameron Highlands.

2. Description of the Study Area

The study area is located between the latitudes of 4°24′37″N–4°33′19″N and the longitudes of 101°20′21″E–101°26′50″E, covering an area of 38.4 km^2 (Figure 1). The geomorphology of the area is characterized by a rugged topography with hill ranges varying from 840 to over 2100 m.a.s.l. The Bertam and Telom Rivers are the main drainage features in this area. Its valleys and tributaries mainly flow from north-northwest to south-southeast [40]. The annual rainfall is between 2500 and 3000 mm per year falling mostly in March and May and also from November–December. The average daytime and nighttime temperatures are 24 °C and 14 °C, respectively, which lie in moderate climatology category. The Cameron Highlands are usually cloud-covered during the year. The tropical forest and tea plantations, temperate vegetable and flower farms are the major crops in the study area [4]. Geologically, megacrystic biotite granites are the most common geological structures of the central mountain chain in Peninsular Malaysia. Schists, phyllite, slate and limestones comprise a significant lithology of Cameron Highlands [81]. Figure 2 shows the geological map of the study area. In Cameron Highlands, most of the landslides have occurred when the maximum daily rainfall reached about 208 mm [82].
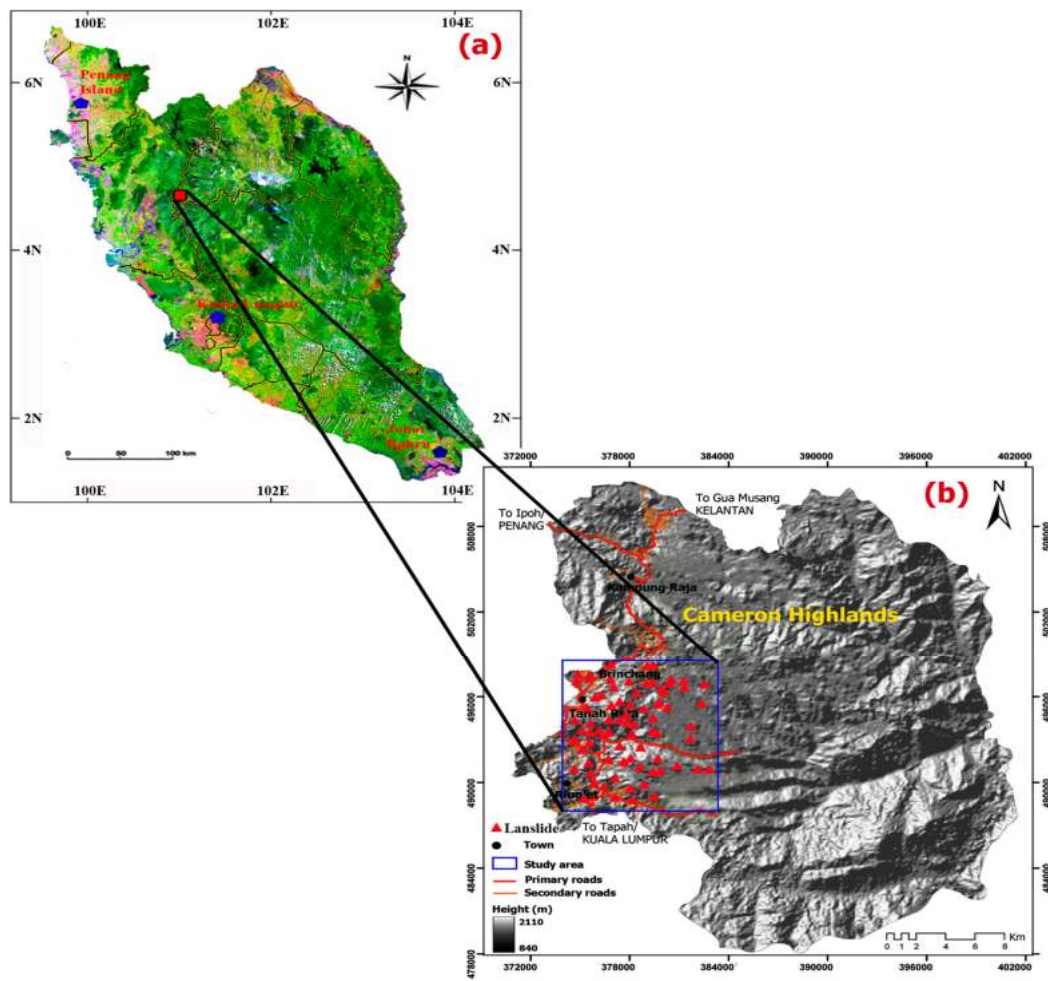
Figure 1. Location of the study area in Cameron Highlands, Peninsular Malaysia; (**a**) Landsat ETM+ mosaic image of Peninsular Malaysia; (**b**) the shaded relief map of Cameron Highlands derived from a 30-m ASTER GDEM modified from Razak [8]. The rectangular area is the actual study area.
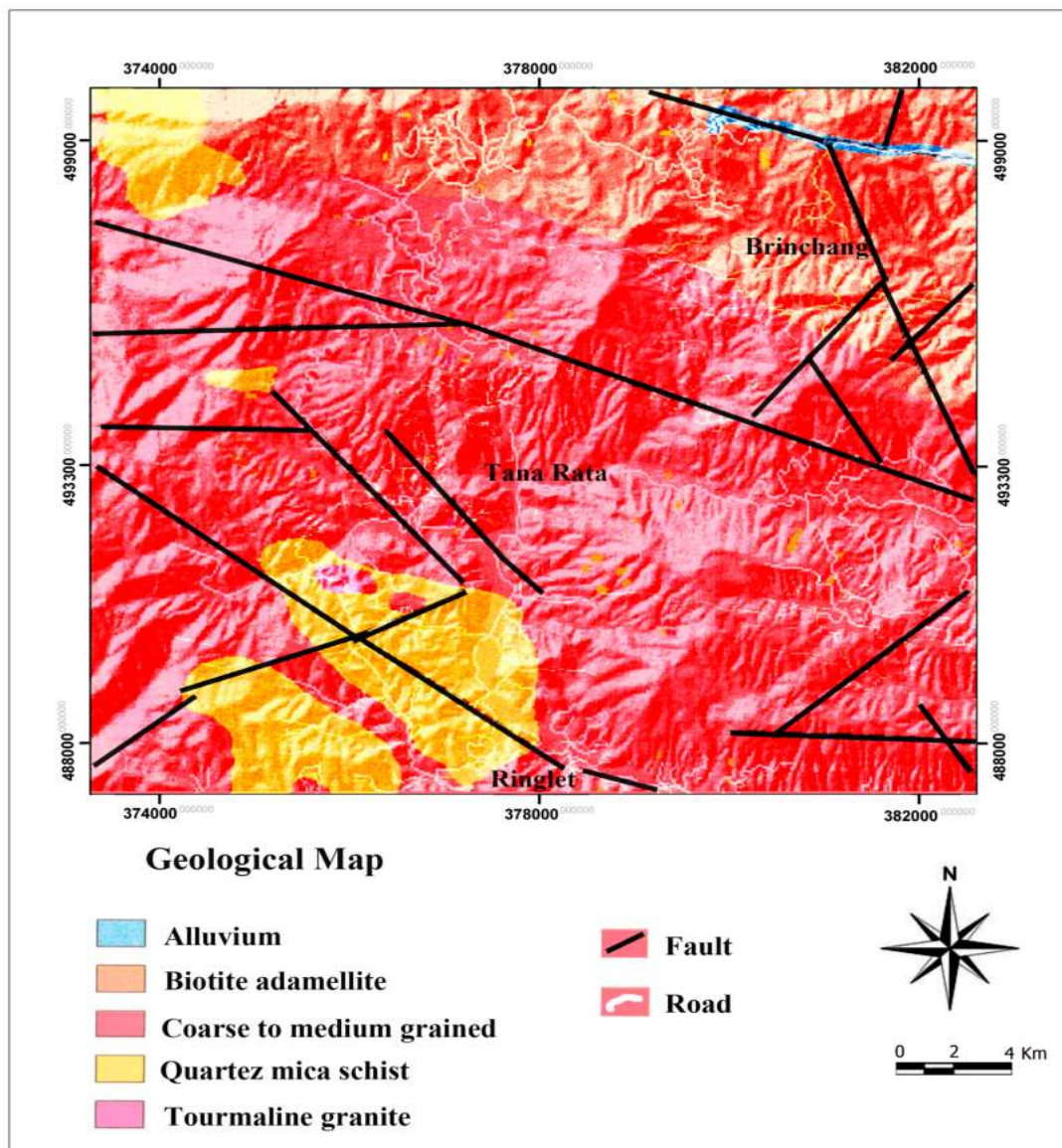
Figure 2. The geological map of a part of the region of the Cameron Highlands as the study area.

3. Materials and Methods

3.1. Landslide Inventory Map

It is difficult to map landslides in the tropical mountainous environments because dense vegetation obscures landslides soon after their occurrence [8]. To obtain important information from landslide locations, remote-sensing data such as aerial photography interpretation and optical satellite images (OSI) are required [19]. The landslide information taken from remotely-sensed images is especially associated with the plant life, morphology and hydrologic conditions of the region [83]. In this study, the interpretation of digital aerial photographs (DAP) with a 10,000–1:50,000 scale over a 25-year period, WorldView-1 satellite imagery (March 2013), AIRSAR data (November 2004), published reports and field surveys has been done for the extraction of the landslide inventory map.

The black and white digital aerial photographs (acquired from the Malaysian Surveying and Mapping Department archives) with a spatial resolution of 0.54 m were taken during 1981–2006. In order to detect the landslides that have occurred in the research area, six digital aerial images were used, and only one block of adjustment was required for the process; 4 stereo models were then formed.

WorldView-1 satellite data with a resolution of 0.46 m were used for the detection of landslides that have occurred and validation of the landslide inventory map. The AIRSAR data, with a 40-MHz, 10-km swath width and slant-range resolution 5 m were collected in November 2004 during the PacRim1 campaign. A DEM (digital elevation model) with a resolution of 10 m combined with C-, L- and P-band images was used to compare with landslide features obtained from digital aerial photographs and WorldView-1 satellite imagery. Although we had some data sources with different scales, all the data were mapped at a resolution of 10 m × 10 m to remove the effect of scale on the detection and validation process. The literature review pinpointed that some researchers have successfully used specified resolutions such as 10 m and 20 m for landslide detection and modeling [4,8].

Table 1 lists the main characteristics of the AIRSAR DEM and WorldView-1 satellite imagery used for landslide detection in the study area.

In the study area, due to the dense forest canopies, the cloudy and rainy weather conditions and also the harsh topography, comprehensive field works and investigations were not possible. Therefore, we had to limit field investigations (ground control points (GCPs)) only to partial locations where they were easily accessible for checking such as along roads and highways, residential areas and the slopes with low elevations. Figure 3 shows landslide types according to the landslide classification of Varnes et al. (1978) [84].

Figure 3. Field photographs of recent landslides and types of landslides: (**a**) a shallow translational rockslide, (**b**) a shallow translational slide at the road side, (**c**) a rotational slide and (**d**) deep-seated rotational slide. The arrow depicts the movement direction.

In order to identify landslides, three techniques were employed: (i) overlaying of landslide vector images onto the DEMs and AIRSAR raster images; (ii) classifying of the images using ENVI 4.8 software; and (iii) separating landslides from the other land cover types using the segmentation tool in "eCognition" software [85]. The spectral values of the C-, L- and P-bands and average slope of the area were used in segmentation as the information about the group of pixels inside the boundaries of the landslide. Besides, the efficiency and quality of optical satellite images and AIRSAR data were examined using root mean square error (RMSE) [85,86].

Table 1. Characteristics of AIRSAR DEM data and WorldView-1 satellite imagery used in the research.

	Date (dd/mm/yy)	Date Type	Band	Polarization	Bytes	Resolution
AIRSAR DEM	9/11/2004	DEM data: Integer 2	C-band	DEM file	25	10 m × 10 m
	9/11/2004	DEM-related data: Integer 2	C-band	VV	25	10 m × 10 m
	9/11/2004	Polarimetric data	L-band	HH, HV, VH, VV	15	10 m × 10 m
	9/11/2004	Polarimetric data	P-band	HH, HV, VH, VV	15	10 m × 10 m
WorldView-1	8/03/2013	Standard (2A)/ortho ready standard (OR2A)	4-band multispectral (BLUE, GREEN, RED, NIR1)	Sun-synchronous	11 bits	0.46 m × 0.46 m
	8/03/2013	Ortho ready stereo	4-band bundle (PAN, BLUE, GREEN, RED, NIR1)	Sun-synchronous	11 bits	0.46 m × 0.46 m

It is noted that the observed landslides are points, while the detected landslides are polygons. In this study, each polygon was finally converted to a point using the "polygon to point" tool in ArcGIS, which represents a pixel of 10 m × 10 m in size. Consequently, the final landslide inventory map was converted to grid format with a cell size of 10 m. A total of 92 landslides were taken into account, among which 74 cases (80%) were selected for training models and the remaining 18 cases (20%) were used for validation purposes. The area of landslides in Cameron Highlands based on obtained landslide inventory is 6.27 km^2, accounting for 4.05% of the entire study area. The maximum, mean and the minimum landslide areas are 0.123, 0.017 and 0.003 km^2, respectively. In addition to landslide locations, we randomly selected 92 non-landslide locations (stable) using the "Create random point" tool in ArcGIS for modeling by SVM in WEKA 3.7.12 software. Then, these points were randomly classified into 80% (74 locations) and 20% (18 locations).

3.2. Landslide Geodatabase

The DEM image was warped to the given ground control points in order to geo-reference the data. Then, the image was further resized equal to the size of the sample area. At this stage, the pixel resolution size was changed to a new resolution of 2 m. The whole resultant sample area DEM heights were then used for comparison with heights of DAP, DEM, GPS and GCPs in the assessment and correction processes. The sequence of procedures and the resultant images are shown in Figure 4.

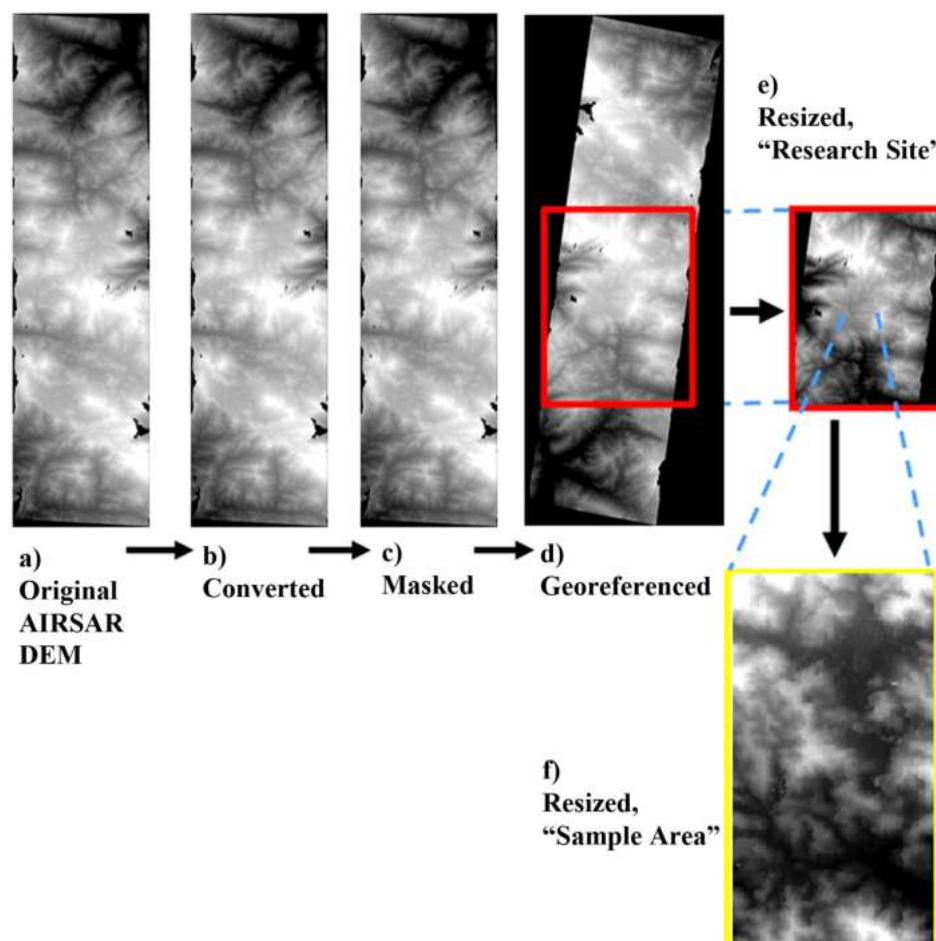**Figure 4.** Sequence of the AIRSAR DEM process: (**a**) opened C-band DEM, (**b**) converted DEM to actual height values, (**c**) masked DEM image, (**d**) geo-referenced, (**e**) resized DEM to the size of research site and (**f**) resized sample area.

For the single C-band VV, the file opened in ENVI 4.8 software was then converted to sigma zero (σ°) and finally to decibels (dBs). Later, this converted Cvv polarization data were combined with the L- and P-band polarimetric data into a single file. Together, they were then masked, corrected from Antenna Pattern Correction (APC) and geo-referenced. The L- and P-band files were opened in ENVI 4.8 software using the POLSAR Tools menu. The process was to decompress (synthesize) the Stoke matrix files into six wavelength-polarization files that include: (1) L band; HH, HV and VV polarization and (2) P band; HH, HV and VV polarization. After processing, the synthesized L and P data were combined with the converted Cvv data into a new single file [87].

Landslide Conditioning Factors

It is important to extract relevant landslide conditioning factors to construct a spatial database [88]. In this study, ten conditioning factors such as slope, aspect, soil, lithology, NDVI, land cover, rainfall, distance to fault, distance to river and distance to road were used to construct a spatial database using ArcGIS. The description of these conditioning factors is shown in Table 2.

As mentioned above, a digital elevation model (DEM) with a 10-m pixel size was produced using AIRSAR DEM (Table 2) from which slope, aspect and distance to river were extracted. Slope, aspect and distance to river factors were then classified into five, nine and seven classes, respectively based on the natural break classification scheme [30] (Table 3). The distance to fault and lithology were derived from the geological map at the 1:63,300 scale, which were classified into six and two classes, respectively (Table 2). The distance to the road was calculated using the topography map with a 50-m buffer zone, which was determined based on the landslides that occurred regarding the closeness of the road in five classes. The soil types were obtained from the soil map at the scale of 1:25,000 and were classified into two classes (Table 3).

Land cover was extracted from the SPOT 5 satellite image using the maximum-likelihood classification method, justified by field survey and in eight classes. The NDVI map was also extracted from SPOT 5 satellite image and in ten classes. The historical rainfall data during the last 30 years was prepared (1981–2011). The average annual rainfall map was prepared with the kriging method using ArcGIS and in ten classes (Tables 2 and 3).

Table 2. Factors used in susceptibility assessment, data sources and associated factor classes for landslide susceptibility mapping in Cameron Highlands.

Spatial Database	Data Layers	Source of Data	GIS Spatial Database	Derived Map	Scale or Resolution
Landslide inventory	Landslide inventory	AIRSAR data, optical satellite images, digital aerial photos and field work	Point and polygon	Seed cells	10-m pixel size
Topographic map	Slope	AIRSAR DEM	GRID	Slope gradient (in degrees)	10-m pixel size
	Aspect	AIRSAR DEM	GRID	Slope orientation	10-m pixel size
Soil	Soil	Soil map	Polygon	Soil	1:25,000
Geology map	Lithology	Geological map obtained from the Mineral and Geosciences Department of Malaysia	ARC/INFO coverage	Lithology	1:63,300
	Fault	Geological map obtained from the Mineral and Geosciences Department of Malaysia	Line	Distance to fault	1:63,300
Road	Road	Topography map	Line	Distance to road	1:25,000
Land use type	Land use	SPOT 5 satellite image	ARC/INFO GRID	Land use	15 m
Normalized difference Vegetation index (NDVI)	NDVI	SPOT 5 satellite image	ARC/INFO GRID	NDVI	15 m
Rainfall	Rainfall	30 years of historical rainfall data	GRID	Rainfall map (mm)	1:25,000
River	Rivers	AIRSAR DEM	ARC/INFO line coverage	Distance to river	10-m pixel size

Table 3. Landside influencing factors and their classes.

	No.	Landslide Causal Factors	Classes
Topographic factors	1	Slope (o)	(1) 0–10; (2) 10–20; (3) 20–30; (4) 30–40; (5) >40
	2	Aspect	(1) Flat; (2) north; (3) northeast; (4) east; (5) southeast; (6) south; (7) southwest; (8) west; (9) northwest
Hydrological factors	3	Rainfall (mm)	(1) 2612–2661; (2) 2662–2678; (3) 2679–2694; (4) 2695–2708; (5) 2709–2719; (6) 2720–2731; (7) 2732–2743; (8) 2744–2754; (9) 2755–2764; (10) 2765–2781
	4	Distance to rivers (m)	(1) 0–50; (2) 50–100; (3) 100–150; (4) 150–200; (5) 200–300; (6) 300–500; (7) >500
Lithological factors	5	Lithology	(1) Metamorphic rock; (2) igneous rock
	6	Distance to faults (m)	(1) 0–50; (2) 50–100; (3) 100–150; (4) 150–200; (5) 200–500; (6) >500
	7	Soil	(1) Serong series; (2) alluvium-colluvium
Land cover factors	8	Land use	(1) Grass; (2) primary forest; (3) rubber; (4) cutting; (5) secondary forest; (6) settlements; (7) agriculture area; (8) water body
	9	NDVI	(1) [(−0.774)–(−0.613)]; (2) [(−0.618)–(−459)]; (3) [(−0.457)–(0.303)]; (4) [(−0.309)–(−0.139)]; (5) [(−0.144)–(0.012)]; (6) [0.015–0.174]; (7) [0.172–0.328]; (8) [0.322–0.491]; (9) [0.491–0.648]; (10) [0.641–0.809]
Man-made factors	10	Distance to roads (m)	(1) 0–50; (2) 50–100; (3) 100–200; (4) 200–500; (5) >500

The flowchart designed in this study for the landslide susceptibility mapping and spatial data is shown in Figure 5. This flowchart includes four parts: (1) landslide conditioning factors (data collection), (2) the landslide inventory map obtained by overlying the observed and detected landslides, (3) the landslide susceptibility mapping by the SVM and IOE models and (4) model analysis and comparison by statistical measures, AUCROC and statistical tests (Friedman and Wilcoxon signed rank tests).
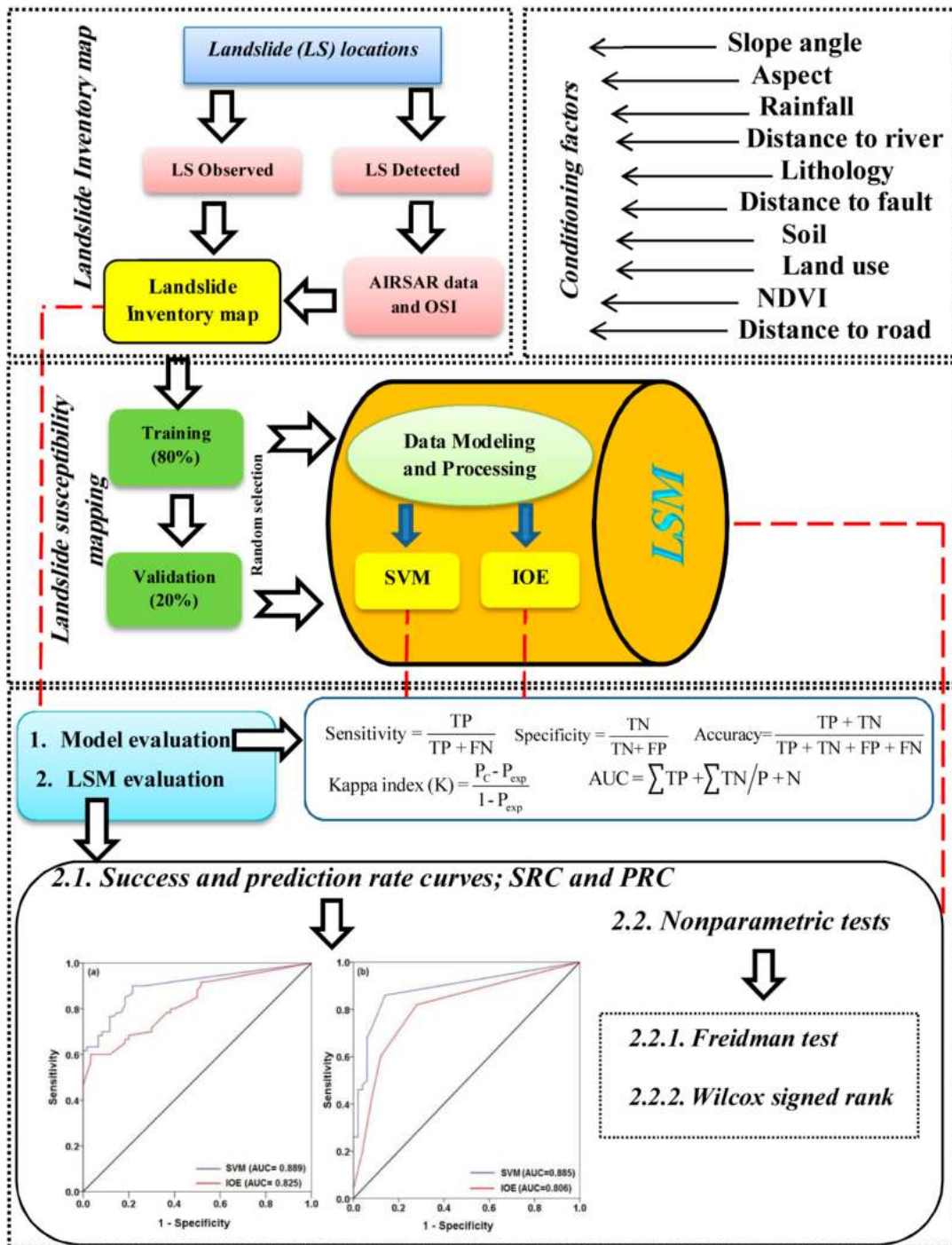
Figure 5. Flowchart of preparing the map for landslide susceptibility mapping. IOE, index of entropy.

3.3. Landslide Susceptibility Models

3.3.1. Support Vector Machine

One of the most popular machine learning algorithms is SVM as a supervised learning binary classifier, which works based on the structural risk minimization principle [89,90]. In the classification issue, the SVM separates a given training dataset based on a hyper-plane to maximize the distance between them, which is known as the maximal margin hyper-plane [89]. Indeed, the aim of SVM is to

find an n-dimensional hyper-plane differentiating between two types by their maximum gap [91,92]. The mathematical expressions are as follows [93]:

$$1/2\|w\|^2 \tag{1}$$

$$y_i((w \cdot x_i) + b) \geq 1 \tag{2}$$

where $\|w\|$ is the norm of the normal hyper plane and b is a constant. After multiplying the Lagrangian coefficient (λ_i), the cost function can be expressed as:

$$L = 1/2\|w\|^2 - \sum_{i=1}^{n} \lambda_i(y_i((w * x_i) + b) - 1) \tag{3}$$

For the non-separable case, the slack variable [94], Equation (4) can be modified as:

$$y_i((w * x_i) + b) \geq 1 - \xi_i \tag{4}$$

After that, v (0, 1), which expresses the misclassification [95], Equation (5) can be defined as:

$$L = \frac{1}{2}\|w\|^2 - \frac{1}{vn}\sum_{i=1}^{n} \xi_i \tag{5}$$

Besides, a kernel function $K(x_i, x_j)$ is taken into account for the nonlinear decision boundary [94]. In this study, the radial basis function (RBF) was selected as the kernel function because of its robustness published by researchers [96,97]. The RBF Gaussian kernel is expressed as follows:

$$K(x_i, x_j) = \exp\left(-\gamma\|x_i - x_j\|^2\right), \gamma > 0 \tag{6}$$

where γ is a parameter of the kernel functions [95].

3.3.2. Index of Entropy

Entropy indicates the extent of the uncertainty of a system [98]. The entropy of landslides indicates the extent of various factors affecting the landslide occurrence [99,100]. We can use the entropy value to calculate the objective weights of the index system [2,101]. The index of entropy (IOE) allows estimating the weight for each conditioning factor (W_j) using the equation as follows [99]:

$$P_{ij} = \frac{b}{a} \tag{7}$$

$$(P_{ij}) = \frac{P_{ij}}{\sum_{j=1}^{S_j} P_{ij}} \tag{8}$$

where a and b are percentages of the study area and landslide, respectively; S_j is called for the class j; (P_{ij}) is the probability density. Here, H_j and H_{jmax} are entropy values (Equations (9) and (10)).

$$H_j = -\sum_{i=1}^{S_j} (P_{ij}) \log_2(P_{ij}), \, j = 1, \, 2, \ldots, \, n \tag{9}$$

$$H_{j\max} = \log_2 S_j \tag{10}$$

where S_j is the number of classes, I_j is the information coefficient (Equation (11)) and W_j is the corresponded weight value of this information coefficient (Equation (12)).

$$I_j = \frac{H_{j\max} - H_j}{H_{j\max}}, I = (0, 1), j = 1, \ldots, n \tag{11}$$

$$W_j = I_j \times P_j \tag{12}$$

The final calculation result of weight values for each parameter is shown in Table 3. Then, the landslide susceptibility map is generated by applying Equation (13) in ArcGIS

$$Y_{IOE} = \sum_i^n \frac{z}{m_i} \times C \times W_j \tag{13}$$

where Y_{IOE} is the total classes; i is the number of map parameters (1, 2, $\ldots$, n); z is the greatest number of classes; m_i is the number of classes within the map parameter; C is the second classified value of class; and W_j is the weight of a parameter [51]. This summation shows the various levels of the landslide susceptibility [101].

3.4. Model Validation and Comparison

3.4.1. Statistical-Based Measures

Statistical index-based methods are used to evaluate and compare the performance of machine learning models. In this study, sensitivity (recall), specificity, precision (positive predictive value (PPV)), accuracy, root mean squared error (RMSE) and chosen Kappa were utilized. According to their formulas, they are defined based on the four types of possible consequences including true positive (TP), false positive (FP), true negative (TN) and false negative (FN). The TP and FP are defined as the proportion of the number of pixels that are correctly classified as landslide and non-landslide, respectively. Meanwhile, TN and FN are the number of pixels classified correctly and incorrectly as non-landslide, respectively [102]. Hence, sensitivity (recall) is defined as the number of correctly-classified landslides per total predicted landslides, while specificity is the number of incorrectly-classified landslides per total predicted non-landslides [102]. Accuracy is the proportion of landslide and non-landslide pixels that are correctly classified [103]. Kappa shows the reliability of the landslide models [103]. It varies from -1 (non-reliable) to 1 (reliable) [60]. If it is $\leq$0, 0–0.2, 0.2–0.4, 0.4–0.6, 0.6–0.8 and 0.8–1, it indicates poor, slight, fair, moderate, substantial and almost perfect agreement between estimation (the model) and observation (the reality), respectively [104]. RMSE shows the error metric between the observed and estimated data of models [103]. The smaller the RMSE, the better performance of the landslide model [105]. Accuracy, sensitivity, specificity, Kappa and RMSE are obtained as follows:

$$\text{Precision} = \frac{\text{TP}}{\text{TP} + \text{FP}} \tag{14}$$

$$\text{Sensitivity} = \frac{\text{TP}}{\text{TP} + \text{FN}} \tag{15}$$

$$\text{Specificity} = \frac{\text{TN}}{\text{TN} + \text{FP}} \tag{16}$$

$$\text{Accuracy} = \frac{\text{TP} + \text{TN}}{\text{TP} + \text{TN} + \text{FP} + \text{FN}} \tag{17}$$

$$\text{kappa} = \frac{\text{P}_{\text{obs}} - \text{P}_{\text{exp}}}{1 - \text{P}_{\text{exp}}} \tag{18}$$

where P_{obs} is the observed agreements; P_{exp} is the expected agreements.

$$P_{obs} = TP + TN/n \tag{19}$$

$$P_{exp} = (TP + FN)(TP + FP) + (FP + TN)(FN + TN)/\sqrt{N} \tag{20}$$

where N is the number of total training pixels; n is the proportion of pixels that is correctly classified.

When the Kappa value is close to 1, this means a perfect agreement between the model and reality. In contrast, a Kappa value close to 0 indicates that the agreement is no better than chance. The worst case is that the agreement is worse than chance with negative kappa. The value has real meaning only when the categories of the two maps depict the same kind of data with the same data classes [106]. Therefore, the kappa index value was also considered to be evidence to show the similarity between the two landslide susceptibility maps.

$$RMSE = \sqrt{\frac{1}{n}\sum_{i=1}^{n}(X_{predicted} - X_{actual})^2} \tag{21}$$

where n is the total sample in the training dataset or the validation dataset; $X_{predicted}$ is the predicted values in the training dataset or the validation dataset; and X_{actual} is the actual (output) values from the landslide susceptibility models.

3.4.2. ROC Curve Analysis

The receiver operating characteristic curve in all landslide susceptibility studies has been applied to evaluate the performance of the models. It is a standard tool that is plotted using sensitivity on the x-axis and 100-specificity on the y-axis [62,105]. The area under the ROC curve (AUC) is commonly used for evaluating the performance of the landslide models [107]. It has a range from 0.5–1; an ideal model has AUC equal to 1, and an inaccurate model has an AUC equal to 0.5 [102]. The AUC is computed using the following equation:

$$AUC = \frac{(\sum TP + \sum TN)}{(P + N)} \tag{22}$$

where TP is the number of landslides that is correctly classified, TN is the number of incorrectly-classified landslides, P is the total number of landslides and N is the total number of non-landslides.

3.5. Statistical Tests (Friedman and Wilcoxon)

The core of this section is the comparison of the performance of two or more machine learning classifiers on multiple datasets using statistical tests. Indeed, the aim is to find which one of these techniques differs statistically in performance without record of their variance. Hence, it is assumed that the compiled results obtained from the machine learning classifiers in this study provide reliable estimates. All classifiers were evaluated using the same random samples. Statistically, there are two methods for the comparison of two or more classifiers including parametric and non-parametric methods. D'Arco et al. (2012) stated that the parametric tests are suitable when the data are normally distributed with equal variances [108]. Additionally, Derrac et al. (2011) reported that the non-parametric tests are free from any statistical assumptions. Moreover, Demšar (2016) expressly declared that non-parametric tests such as Friedman and Wilcoxon sign rank tests are safer and their results stronger than parametric tests, since they do not assume normal distributions or homogeneity of variance.

For this reason, in this study, Freidman [109] and Wilcoxon [110] signed rank tests were used to compare the significant differences between the treatments of models. The null hypothesis for them is that there are not any differences between the performances of the landslide models at the significance

level of α = 0.05 (or 5%). Then, a judgement is made based on the probability of a hypothesis (*p*-value), so that if the *p*-value is true, the null hypothesis is rejected, and as a result, there is a significant difference between the two models and vice versa [62]. It is probably in the comparison process between two or more models that the *p*-value in the Friedman test for all models was true. In this case, the result is not reliable to compare between models [62]. Therefore, the strategy used in this case is the Wilcoxon signed-rank to assess the statistical significance of systematic pairwise differences between the landslide models. In this test, the *p*-value and z-value are used for evaluating the significance of differences between the landslide susceptibility models. When the *p*-value is less than 0.05 and the z-value exceeds the critical values of z (-1.96 and $+1.96$), the null hypothesis is rejected, and thus, the performance of the susceptibility models is significantly different [62–64].

4. Results and Analysis

4.1. Landslide Detection Using AIRSAR and Optical Satellite Images

The classified section of the segmented image overlaid onto the old landslide map is shown in Figure 6a–c. According to this figure, the detected landslides have relatively good concordance with polygons (observed) classified as landslides. Two processes were conducted in order to validate the location of the detected landslides. The first was WorldView-1 satellite images and digital aerial photographs and the other was field surveying. Field observation was then carried out to check the locations of the landslides shown in the old landslide map (Figure 6a). The results exploited that identification of landslides is difficult on the ground due the small size, no traces and also covering of scars by dense vegetation (Figure 6b). The time difference between the production of the map (2004) and the field observation (2015) could be another reason (Figure 6c).
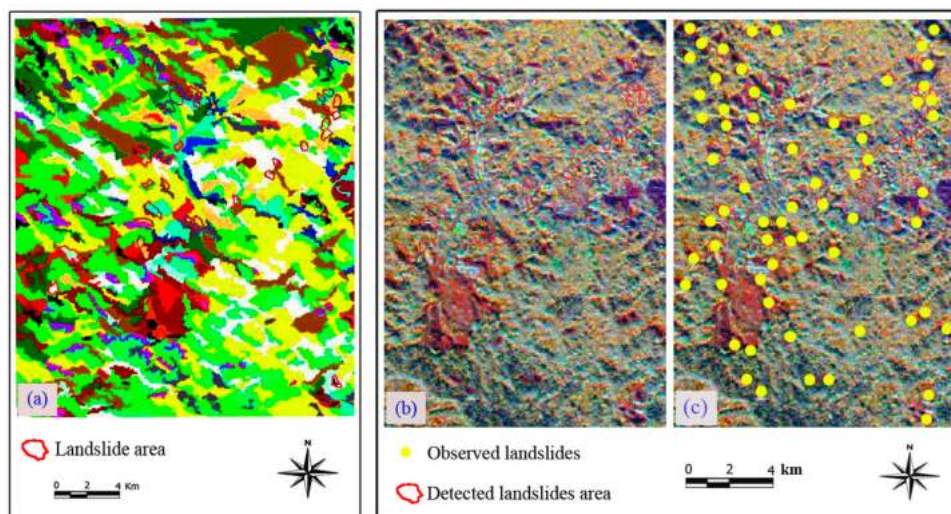

Figure 6. The AIRSAR composite image is overlaid onto the old landslides map: (**a**) the segmented and classified AIRSAR images overlaid with the old landslide map (landslides in red polygons), (**b**) detected landslides and (**c**) comparing detected and observed landslides.

The landslide features obtained from WorldView-1 satellite images were overlaid onto the C-, L- and P-band images. Hence, the landslide inventory map was validated by WorldView-1 satellite images and digital aerial photographs. C-, L- and P-band images were used in the UTM reference system for the landslide features. The final compiled landslide inventory map in this study is shown in Figure 7. The comparison between Figures 6 and 7 confirms that landslides detected by AIRSAR data have almost a logical concordance with the old landslides in the study area. It is noticed that the gray color in Figure 7 only indicates the elevations as a hillshade map over the study area.
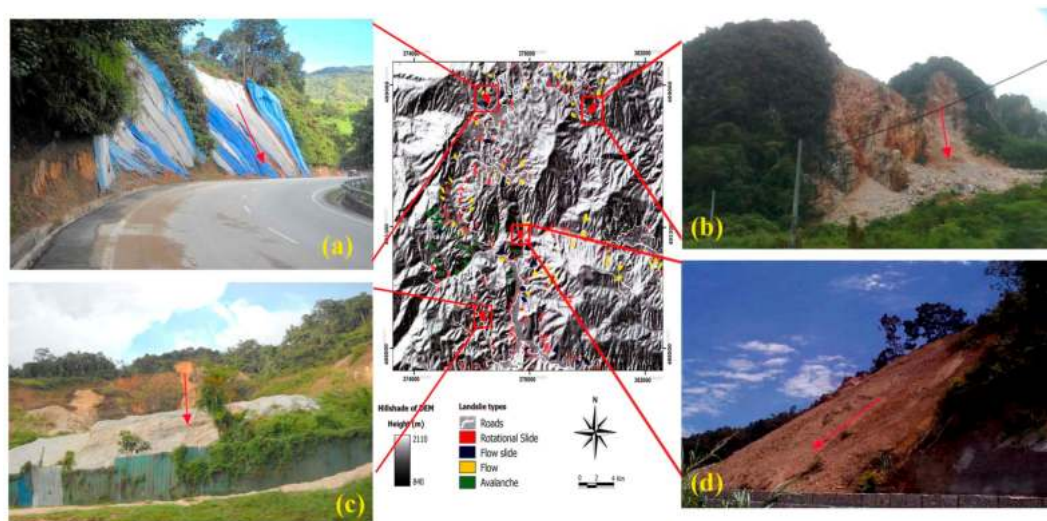
Figure 7. Final landslide inventory map: (**a**) a translation slide, (**b**) a shallow translational rockslide, (**c**) a rotational slide and (**d**) a translation slide.

It should be noted that the total of 92 landslide locations in this study was selected based on the overlaying between the detected and observed landslides for landslide modeling. As a final result, the validity of the detected and observed landslides using RMSE concluded that the different between them was 0.163 (16.3%), which is a reasonable result.

4.2. Model Analysis and Results

The results of the performance of the SVM and IOE models using training and validation datasets are shown in Table 4. Landslide modeling in the training phase concluded that the SVM model had the highest sensitivity (94.6%), illustrating that 94.6% of the landslide pixels were correctly classified in the landslide class, followed by the IOE model (87.8%). Furthermore, results revealed that the highest specificity (87.8%) belonged to the SVM model, indicating that 87.8% of the non-landslide pixels were correctly classified with respect to the non-landslide class, followed by the IOE model (79.2%). Additionally, the SVM model had the highest value of accuracy (91.2%), Kappa (0.883) and AUC (89.6%) compared to the IOE model.

Overall, the SVM and IOE models were both successfully trained in the training phase. However, the SVM model was more accurate than the IOE model in the model construction procedure. The landslide susceptibility indexes were calculated for all pixels in the study area using these models to obtain landslide susceptibility mapping.

Table 4. Model performance on the training and validation datasets for the SVM and IOE models.

	Training		Validation	
Train	SVM	IOE	SVM	IOE
True positive (TP)	70	65	16	14
True negative (TN)	65	61	14	13
False positive (FP)	9	16	4	5
False negative (FN)	4	9	2	4
Sensitivity (%)	94.6	87.8	88.9	77.8
Specificity (%)	87.8	79.2	77.8	72.2
Accuracy (%)	91.2	83.4	83.3	75.0
Kappa	0.883	0.813	0.663	0.613
AUROC	0.896	0.826	0.845	0.826

4.3. Model Validation and Comparison

After model construction, the validation of the models was performed using the validation dataset based on the area under the ROC curve, the kappa index and the statistical evaluation measures (Table 4). The results depicted that the two landslide models showed a high predictive capability for spatial prediction of landslides in the study area. Moreover, the comparison results showed that the SVM model had the highest sensitivity (88.9%), indicating that 88.9% of the landslide pixels were correctly classified in the landslide class, followed by the IOE model (77.8%). The SVM model also had the highest value of specificity (77.8%), indicating that 77.8% of the non-landslide pixels were correctly classified with respect to the non-landslide class. Additionally, the results of model validation and comparison revealed that the highest accuracy (0.833), Kappa (0.663) and AUC (0.845) belonged to the SVM model, followed by the IOE model with the values of 0.750, 0.613 and 0.826, respectively. Eventually, the SVM and IOE models were successfully validated in the evaluation process emphasizing that the SVM model had a greater power of prediction in the landslide model validation process.

4.4. Generating Landslide Susceptibility Mapping and Comparison

4.4.1. LSM by SVM Model

In this study, the radial basis function (RBF) was applied as the kernel function, and the two-class SVM models were firstly trained to build the landslide susceptibility map using ArcGIS. Based on the report by Yao et al. (2008), the two-class SVMs can produce a more accurate susceptibility map. The training data were used to train the SVM model [100]. Two main parameters such as c and γ in this model were suggested, 0.8 and 0.5, respectively.

Figure 8 is the landslide susceptibility map prepared by the SVM model. Finally, the landslide susceptibility map extracted from the SVM model was reclassified into four susceptibility classes using the natural breaks method as: low, moderate, high and very high. According to the SVM-derived landslide susceptibility map, the very high susceptible zones yielded about 39.78% (15.27 km^2) of the total area, while about 27.41% (10.52 km^2) was classified as a high susceptibility and 14.92% of the study area (5.72 km^2) as a moderate susceptibility zone. It is noticed that the gray color in Figure 8 only indicates the low and high elevations as a hillshade map over the study area, which has not been analyzed. Seventeen-point-eight-nine percent of the study area (6.86 km^2) is also classified as a low susceptibility zone (Figure 9).
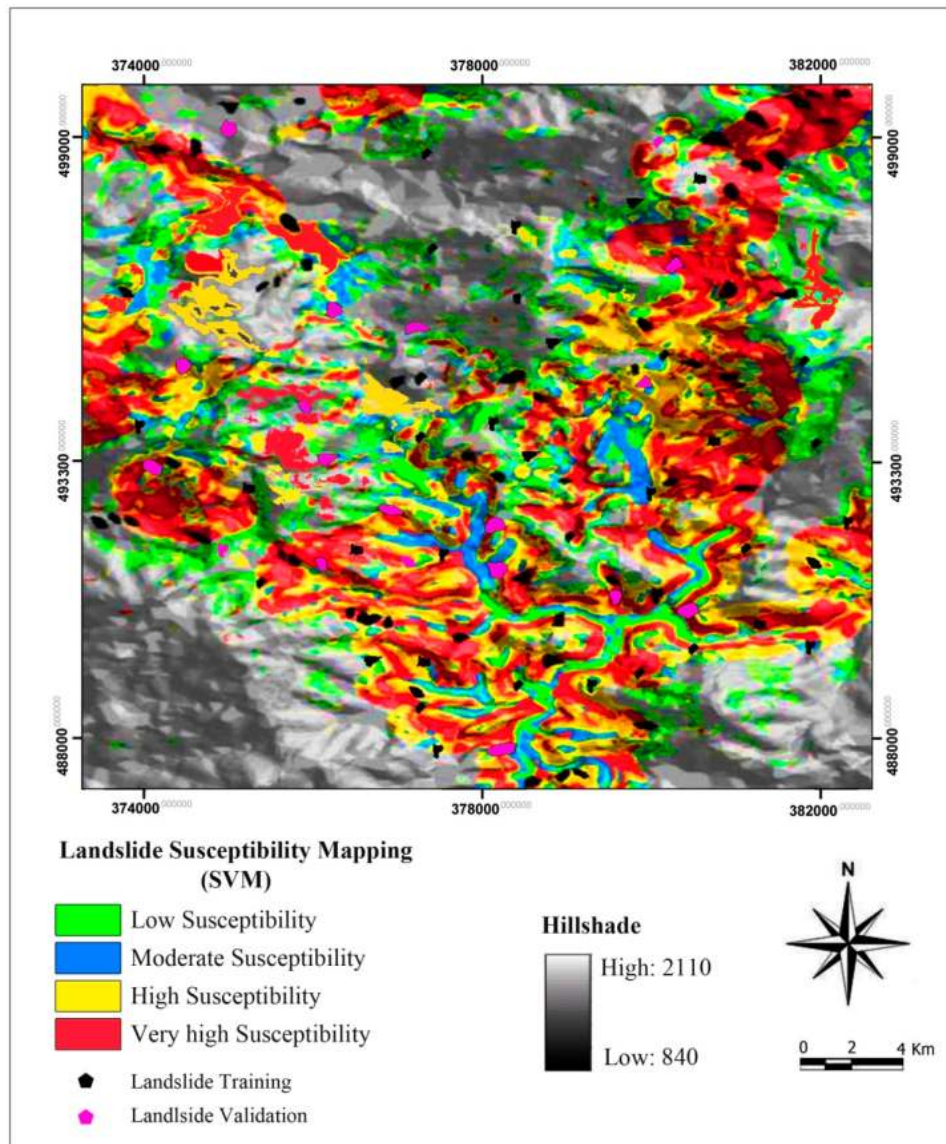
Figure 8. Landslide susceptibility map produced by the SVM model.
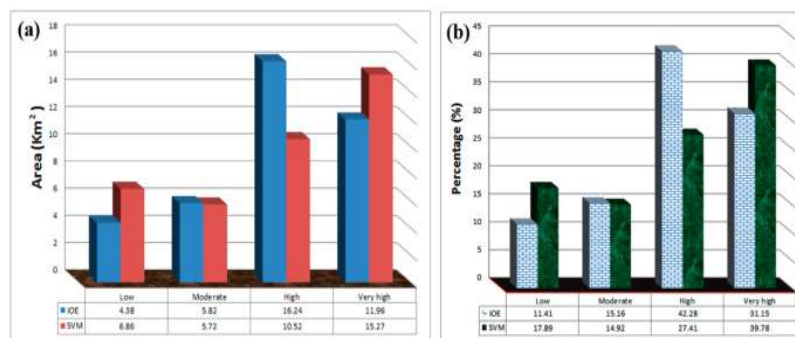
Figure 9. Histograms representing the distribution of observed landslides falling into various susceptibility classes of landslide susceptibility mapping (LSM) extracted from SVM and IOE models: (**a**) area (km^2) of landslides that occurred; (**b**) percentage (%) of landslides that occurred.

4.4.2. LSM by the IOE Model

The landslide susceptibility index was calculated by adding up the weighted multiplications by the secondarily reclassified conditioning factors given by Equation (23).

$$Y_{IOE} = \text{(Slope degree} \times 0.910) + \text{(Aspect} \times 0.840) + \text{(Soil} \times 1.172) + \text{(Lithology} \times 1.127) + \text{(NDVI} \times 0.184) + \text{(Land cover} \times 0.932) + \text{(Rainfall} \times 1.753) + \text{(Distance to fault} \times 0.692) + \text{(Distance to drainage} \times 1.670) + \text{(Distance to road} \times 0.793)} \tag{23}$$

The related weights (W_j) and probability density (P_{ij}) for landslide in each class were calculated using the IOE model shown in Table 5. According to the results (P_{ij}), slope degree classes of 30–40° and 20–30° were highly related to landslides with high values of 0.315 and 0.253, respectively. For aspect, northwest and north-facing slopes were susceptible to landslide occurrence with high values of 0.176 and 0.167, respectively.

Most landslides occurring in soil classes based on (P_{ij}) were alluvium-colluvium and Serong series with high values of 0.507 and 0.492, respectively. The highest (P_{ij}) value of lithology belongs to metamorphic rocks as 0.512. Furthermore, the (P_{ij}) value for the NDVI index indicated that classes of −0.144–0.012 and 0.641–0.809 were prone to landslide occurrence with high values of 0.136 and 0.135, respectively (Table 5). The relationship between land cover and landslide occurrence showed that the values of (P_{ij}) were higher in the classes of agricultural area and settlements with values of 0.180 and 0.129, respectively. The (P_{ij}) values for rainfall, the highest values (0.276 and 0.105), corresponded to the rainfall classifications of 2765–2781 and 2755–2764 mm/year, respectively.

According to the investigation of distance to faults, the (P_{ij}) value decreased once distance to roads increased. In this case, the classes of 0–50 m and 50–100 m had high correlations with landslide occurrence with (P_{ij}) values of 0.257 and 0.169, respectively. Distance to road and distance to drainage were the same as distance to fault such that the (P_{ij}) value decreased, whereas the distance to these features increased. Most of the landslides were located in the classes of 0–50 m and 50–100 m in terms of distance to drainage with (P_{ij}) values of 0.160 and 0.153 and the same classes of distance to road with values of 0.302 and 0.173. Furthermore, according to the W_j value of the IOE model, rainfall (1.753) had the highest influence on the landslide susceptibility, followed by distance to drainage (1.670), soil (1.172), and lithology (1.127), while the others were much less significant for landslide susceptibility assessment in the region. It should be also kept in mind that the landslide conditioning factors may be different in different regions, such that some factors were suitable for this study area, but may not fit other areas [111,112]. In this research, based on the results of the index of entropy (IOE) model, we reclassified the landslide susceptibility map, using the natural break approach, into four categories as low, moderate, high and very high (Figure 10). It is remarkable that the gray color in Figure 10 only indicates the low and high elevations as a hillshade map over the study area, which has not been analyzed.
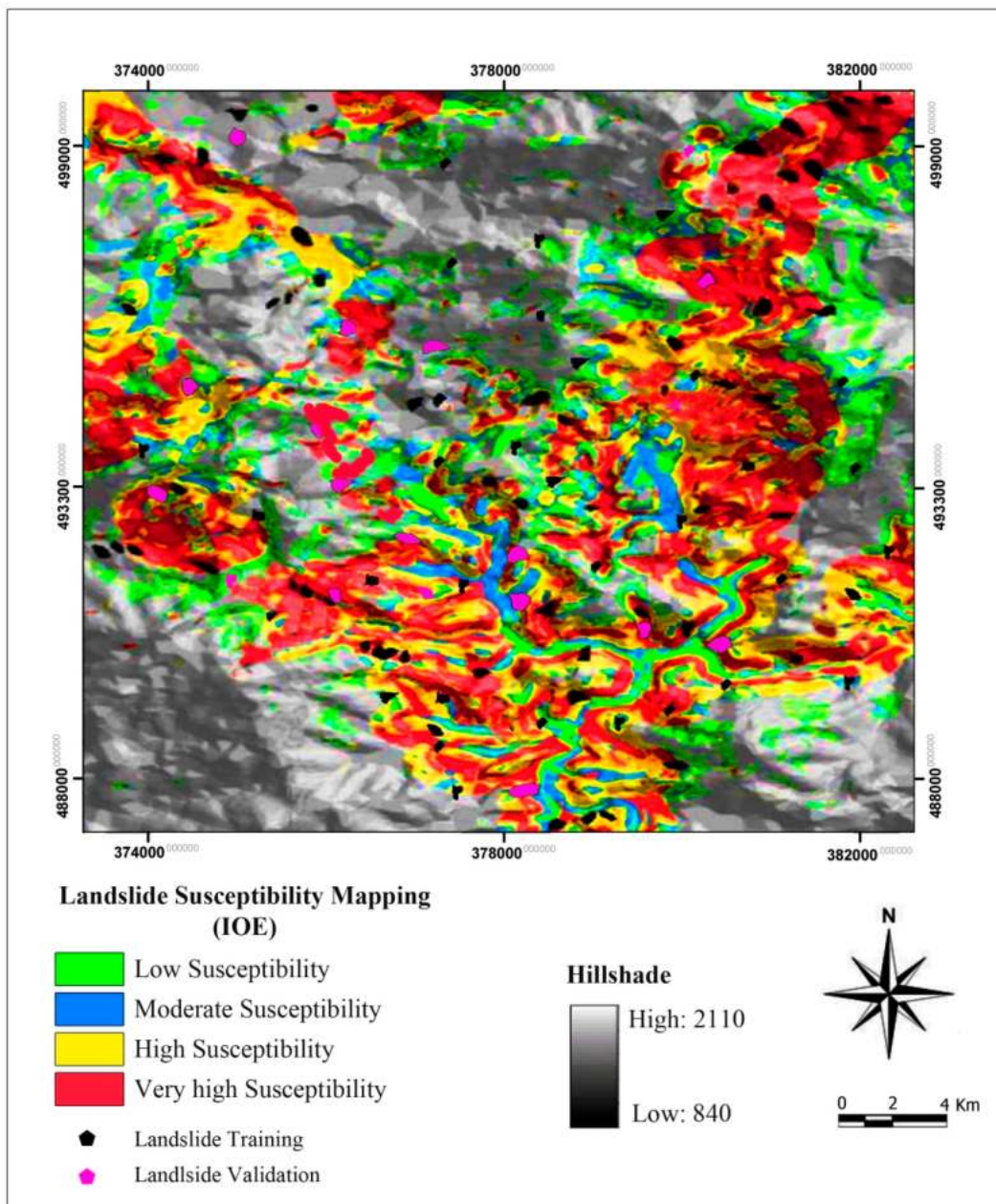
Figure 10. Landslide susceptibility map produced by the IOE model.

Table 5. Spatial relationship between each landslide conditioning factor and landslide by the SVM and IOE models.

Factor	Class	Percentage of Domain	Percentage of Landslide	P_{ij}	(P_{ij})	H_j	H_{jmax}	I_j	W_j
Slope (°)	0–10	17.63	9.07	0.51	0.107	1.085	1.629	0.962	0.910
	10–20	19.45	14.51	0.75	0.158				
	20–30	21.71	26.12	1.20	0.253				
	30–40	25.31	37.84	1.49	0.315				
	>40	15.90	12.46	0.78	0.164				
Aspect	Flat	0.00	0.00	0.00	0.00	1.726	1.871	0.948	0.840
	North	6.09	8.14	1.34	0.167				
	Northeast	16.41	14.39	0.88	0.110				
	East	19.01	21.54	1.13	0.141				
	Southeast	18.93	17.28	0.91	0.114				
	South	10.21	9.46	0.93	0.116				
	Southwest	7.58	3.52	0.46	0.057				
	West	10.15	9.31	0.92	0.115				
	Northwest	11.62	16.36	1.41	0.176				
Soil	Serong series	38.87	38.05	0.98	0.492	1.471	1.938	1.178	1.172
	Alluvium-colluvium	61.13.	61.95	1.02	0.507				
Lithology	Metamorphic rock	58.63	59.72	1.11	0.512	1.718	1.995	1.133	1.127
	Igneous rock	41.37	40.28	0.97	0.487				
NDVI	−0.774–−0.613	0.00	0.00	0.00	0.000	0.701	0.955	0.220	0.184
	−0.618–−0.459	6.41	5.23	0.81	0.096				
	−0.457–−0.303	8.72	7.93	0.91	0.108				
	−0.309–−0.139	12.16	10.33	0.85	0.101				
	−0.144–0.012	26.28	29.95	1.14	0.136				
	0.015–0.174	3.04	2.01	0.66	0.078				
	0.172–0.328	4.96	5.11	1.03	0.123				
	0.332–0.491	7.21	6.76	0.94	0.112				
	0.491–0.648	11.70	10.55	0.90	0.107				
	0.641–0.809	19.52	22.13	1.13	0.135				
Land use	Grass	3.62	2.73	0.75	0.099	1.735	1.899	0.985	0.932
	Primary forest	8.71	12.44	0.74	0.097				
	Rubber	8.11	7.45	0.92	0.121				
	Cutting	21.79	20.47	0.94	0.125				
	Secondary forest	19.62	18.43	0.93	0.122				
	Settlements	18.14	17.76	0.98	0.129				
	Agriculture area	4.46	6.10	1.37	0.180				
	Water body	15.55	14.62	0.94	0.124				

Table 5. *Cont.*

Factor	Class	Percentage of Domain	Percentage of Landslide	P_{ij}	(P_{ij})	H_j	H_{jmax}	I_j	W_j
Rainfall (mm/year)	2612–2661	16.57	15.87	0.96	0.079	1.766	2.239	1.450	1.753
	2662–1681	6.20	6.18	0.99	0.081				
	2679–2694	6.77	6.98	1.03	0.085				
	2695–2708	18.12	19.63	1.09	0.090				
	2709–2719	8.66	7.17	0.83	0.068				
	2720–2731	10.07	8.23	0.82	0.067				
	2732–2743	11.11	9.55	0.86	0.071				
	2744–2754	13.95	12.41	0.89	0.073				
	2755–2764	7.09	9.10	1.28	0.105				
	2765–2781	2.46	4.88	3.34	0.276				
Distance to faults (m)	0–50	11.75	19.23	1.07	0.257	1.378	1.548	0.657	0.692
	50–100	21.19	22.64	1.05	0.169				
	100–150	9.04	9.41	1.04	0.164				
	150–200	10.98	11.79	1.07	0.163				
	200–500	29.71	25.81	0.87	0.137				
	>500	17.33	11.12	0.64	0.101				
Distance to rivers (m)	0–50	11.40	12.91	1.23	0.160	2.558	2.633	1.661	1.670
	50–100	19.41	21.01	1.08	0.153				
	100–150	17.99	18.65	1.03	0.146				
	150–200	3.61	3.72	1.03	0.145				
	200–300	9.33	8.97	0.96	0.136				
	300–500	29.77	27.09	0.91	0.129				
	>500	8.49	7.65	0.90	0.127				
Distance to roads (m)	0–50	22.01	37.64	1.17	0.302	1.611	1.759	0.843	0.793
	50–100	19.26	18.82	0.98	0.173				
	100–150	15.52	11.76	0.76	0.135				
	150–200	13.84	10.61	0.76	0.134				
	200–500	17.98	12.94	0.72	0.127				
	>500	11.39	8.23	0.72	0.123				

Based on the landslide susceptibility map obtained from the IOE model, 11.41% (4.38 km^2) of the entire study area was located in the low landslide susceptibility zone. Moderate and high susceptible zones displayed 15.16% (5.82 km^2) and 42.28% (16.24 km^2) of the total area, respectively. The very high landslide susceptibility zone occupied 31.15% (11.96 km^2) of the total study area, as well (Figure 9).

The capability of the prediction accuracy of the SVM and IOE models was evaluated using the area under the ROC curve (AUROC) based on the training dataset (success rate curve), validation dataset (prediction rate curve) and the Friedman and Wilcoxon signed rank statistical tests. Figure 11 shows the comparison of AUC for the two models using training and validation datasets. Basically, the results of the success rate curve indicated that landslide susceptibility mapping, based on the existing landslide occurrence, using the SVM and IOE models had a good prediction capability. Additionally, the results demonstrated that the SVM model had a higher value of AUC (0.889) compared to the IOE (0.825) model (Figure 11a). Moreover, the results of the prediction rate curve confirm that the landslide susceptibility map plotted by validation landslides, which are supposed to occur in the future, had high prediction accuracy. However, the SVM model showed a high prediction accuracy (AUC = 0.885), followed by the IOE (AUC = 0.806) model (Figure 11b).
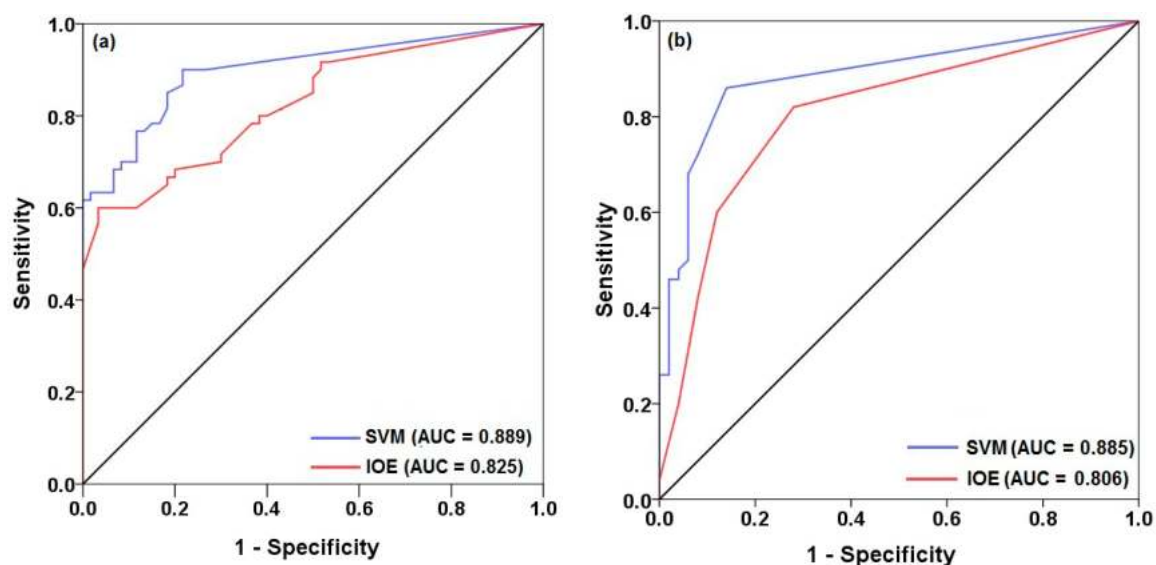

Figure 11. Success and prediction accuracy rate curves of the SVM and IOE models used in landslide susceptibility mapping.

In addition to the AUROC, two statistical tests, the Friedman and Wilcoxon signed rank tests, were applied to validate the landside models. The results of the Friedman test are shown in Table 6. Results indicated that the values of average ranking (AR) for the SVM and IOE models were 2.01 and 1.65, respectively. Although the chi-square was 35.286, due to a significance level of 0.000, the Friedman test was not appropriate for judging the capability of performance between the models. To detect this challenge, the Wilcoxon signed rank test was utilized to assess the pairwise differences between the SVM and IOE models at the 5% significant level (Table 7). Statistically, if there is not a significant difference between the two landslide models at the significant level of 5% (rejection of the null hypothesis), it will be accepted that the results of the two models are not the same.

Table 6. Average ranking of the two landslide susceptibility models using the Friedman test.

Landslide Models	Mean Ranks	χ^2	Significance
SVM	2.01	35.286	0.000
IOE	1.65		

Table 7. Performance of the two landslide susceptibility models using the Wilcoxon signed-rank test.

Pairwise Comparison	Positive	Negative	Z (Value)	*p* (Value)	Significance
SVM vs. IOE	45	12	−10.235	0.000	Yes

The standard *p*-value is 0.05.

Tien Bui et al. (2016) reported that when *p* (value) < 5% (0.05) and z (value) > z (−1.96 and +1.96), it is assumed that the capability of the two models is significantly different [72]. According to Table 7, results concluded that there was a statistical difference between two landslide susceptibility models (*p* (value) = 0.000, z (value) = −10.235, significance = yes).

5. Discussion

On the one hand, due to dense vegetation and cloudy and rainy weather conditions, detection of landslides is a challenging task in the vast and inaccessible mountainous terrain of tropical environments. On the other hand, few studies have attempted to prepare landslide susceptibility mapping using detected landslides by remote sensing data over the world [113,114]. For example, Gorsevski et al. (2016) using LIDAR data detected landslides in the Cuyahoga Valley National Park, Ohio, in order to generate a susceptibility map using the artificial neural networks model [113].

The detection process for achieving the landslide inventory map was carried out using DAP, WorldView-1 satellite imagery and AIRSAR data in the current study. The spectral values of the pixels that represent landslides can be differentiated from those of the surroundings. On the one hand, the spatial resolution of AIRSAR DEM is low (10 m), and on the other hand, the resolution of WorldView-1 satellite imagery is high (0.46 m). Therefore, the composite image is one example among several composite images produced. In general, because of the low resolution and rough topography, it is difficult to differentiate the various land cover types using AIRSAR DEM. The findings conclude that the landslide features obtained from WorldView-1 satellite images that were overlaid onto the C-, L- and P-band images could precisely detect landslides. The validation process of the detected landslides pinpointed that their locations conformed to the ground control points and the observed landslides through the RMSE value. Furthermore, our findings confirm that for a region where identification of landslides is facing a challenge, the application of landslide detection by remote sensing data can be presented as a reasonable solution. Cheng et al. (2011) declared that the extensive remote sensing imagery has a significant role in landslide inventory mapping, landslide susceptibility and hazard mapping using the detection process [115]. Furthermore, Metternicht et al. (2005) have mentioned the role of GIS and RS in landslide detection for spatial prediction of landslides [116].

In this study, we selected a total of 92 landslides using the detection process and checked their locations with the observed landslides for spatial prediction of landslides in Cameron Highlands, Malaysia. Landslide susceptibility mapping was produced using a machine learning algorithm: support vector machine and a statistical method: the index of entropy. For landslide modeling, ten conditioning factors such as slope, aspect, soil, lithology, NDVI, land cover, rainfall, distance to fault, distance to river and distance to road were utilized. The validation process was done using some statistical criteria including sensitivity, specificity, accuracy, Kappa and AUROC based on the training (goodness-of-fit) and validation (performance of models) datasets. The results indicated that the SVM model had a higher goodness-of-fit and performance compared to the IOE model. Additionally, the results of the evaluation of landslide susceptibility maps extracted using the two models by AUROC and two statistical tests including the Friedman and Wilcoxon signed rank tests showed that the SVM model outperformed the IOE model. SVM as a soft computing benchmark model can perform well among the many models for the spatial prediction of landslides [74,96,117,118]. The strength of SVM in comparison to IOE is due to its robustness and ability in removing the over-fitting and noise problems in the modeling process, resulting in increasing the model prediction accuracy.

6. Conclusions

Landslides are very dangerous and destructive disasters all over the world. Therefore, landslide detection is very important for the government and local residents in any country. Cameron Highlands, Malaysia, has a typical landslide problem because of its heavy rainfall and mountainous location. Landslides have frequently occurred in this area following heavy rainfall, specifically in inaccessible areas where field work is difficult to carry out. Hence, the combination of optical and SAR data is a suggested technical strategy for identifying landslides in tropical environments.

The results of the detected landslide and the observed landslides (landslide inventory map) revealed the strong capability of WorldView-1 images and AIRSAR data to detect very small landslides, which occurred due to heavy rainfall with an acceptable RMSE of 0.163 (16.3%). Based on the obtained results from the IOE model, rainfall has the highest influence on landslide occurrence, followed by distance to river, soil, lithology, land cover, slope angle, aspect, distance to road, distance to fault and NDVI. The analysis and validation of the model results using statistical-based measures and AUROC showed that SVM outperformed the IOE model. Additionally, the validation results showed that more than 80% of the total landslide pixels were correctly classified by the IOE and SVM models, indicating the power of prediction of these models in the study area.

Additionally, the results of success and prediction rate curves illustrated that the SVM model had more power of prediction in the determination of existing and future landslides. The current research exploited that the C-, L- and P-band images of AIRSAR data are able to provide acceptable coherence in the study area. Landslide detection in conjunction with GIS susceptibility mapping is proposed for future work based on satellite images with high resolution and more accuracy. The information provided by landslide susceptibility maps could help planners and engineers to make better decisions about landslide prevention, mitigation and avoidance.

Author Contributions: D.T.B., H.S., A.S., K.C., M.A., W.C., B.B.A., A.M., M.P., H.H. and Y.T. contributed equally to the work. H.S. collected field data and conducted the landslide mapping and analysis. H.S., A.S., K.C., M.A., W.C., A.M., M.P., H.H. and Y.T. wrote the manuscript. D.T.B., B.B.A., M.P., H.H. and Y.T. provided critical comments in planning this paper and edited the manuscript. All the authors discussed the results and edited the manuscript.

Conflicts of Interest: The authors declare no conflict of interest.

References

1. Yilmaz, I. Comparison of landslide susceptibility mapping methodologies for Koyulhisar, Turkey: Conditional probability, logistic regression, artificial neural networks, and support vector machine. *Environ. Earth Sci.* **2010**, *61*, 821–836. [CrossRef]
2. Pourghasemi, H.R.; Mohammady, M.; Pradhan, B. Landslide susceptibility mapping using index of entropy and conditional probability models in GIS: Safarood basin, Iran. *Catena* **2012**, *97*, 71–84. [CrossRef]
3. Takara, K.; Yamashiki, Y.; Sassa, K.; Ibrahim, A.B.; Fukuoka, H. A distributed hydrological–geotechnical model using satellite-derived rainfall estimates for shallow landslide prediction system at a catchment scale. *Landslides* **2010**, *7*, 237–258.
4. Pradhan, B.; Sezer, E.A.; Gokceoglu, C.; Buchroithner, M.F. Landslide susceptibility mapping by neuro-fuzzy approach in a landslide-prone area (cameron highlands, Malaysia). *IEEE Trans. Geosci. Remote Sens.* **2010**, *48*, 4164–4177. [CrossRef]
5. Pradhan, B. Landslide susceptibility mapping of a catchment area using frequency ratio, fuzzy logic and multivariate logistic regression approaches. *J. Indian Soc. Remote Sens.* **2010**, *38*, 301–320. [CrossRef]

6. Shahabi, H.; Ahmad, B.; Khezri, S. Evaluation and comparison of bivariate and multivariate statistical methods for landslide susceptibility mapping (case study: Zab basin). *Arab. J. Geosci.* **2013**, *6*, 3885–3907. [CrossRef]

7. Dai, F.; Lee, C.; Ngai, Y.Y. Landslide risk assessment and management: An overview. *Eng. Geol.* **2002**, *64*, 65–87. [CrossRef]

8. Razak, K.A.; Santangelo, M.; Van Westen, C.J.; Straatsma, M.W.; de Jong, S.M. Generating an optimal dtm from airborne laser scanning data for landslide mapping in a tropical forest environment. *Geomorphology* **2013**, *190*, 112–125. [CrossRef]

9. Corominas, J.; Van Westen, C.; Frattini, P.; Cascini, L.; Malet, J.-P.; Fotopoulou, S.; Catani, F.; Van Den Eeckhaut, M.; Mavrouli, O.; Agliardi, F. Recommendations for the quantitative analysis of landslide risk. *Bull. Eng. Geol. Environ.* **2014**, *73*, 209–263. [CrossRef]

10. Ouchi, K. Recent trend and advance of synthetic aperture radar with selected topics. *Remote Sens.* **2013**, *5*, 716–807. [CrossRef]

11. Joyce, K.E.; Belliss, S.E.; Samsonov, S.V.; McNeill, S.J.; Glassey, P.J. A review of the status of satellite remote sensing and image processing techniques for mapping natural hazards and disasters. *Prog. Phys. Geogr.* **2009**, *33*, 183–207. [CrossRef]

12. Teshebaeva, K.; Roessner, S.; Echtler, H.; Motagh, M.; Wetzel, H.-U.; Molodbekov, B. Alos/palsar insar time-series analysis for detecting very slow-moving landslides in southern Kyrgyzstan. *Remote Sens.* **2015**, *7*, 8973–8994. [CrossRef]

13. Corsini, A.; Farina, P.; Antonello, G.; Barbieri, M.; Casagli, N.; Coren, F.; Guerri, L.; Ronchetti, F.; Sterzai, P.; Tarchi, D. Space-borne and ground-based sar interferometry as tools for landslide hazard management in civil protection. *Int. J. Remote Sens.* **2006**, *27*, 2351–2369. [CrossRef]

14. Du, Y.; Xu, Q.; Zhang, L.; Feng, G.; Li, Z.; Chen, R.-F.; Lin, C.-W. Recent landslide movement in tsaoling, taiwan tracked by terrasar-x/tandem-x dem time series. *Remote Sens.* **2017**, *9*, 353. [CrossRef]

15. Plank, S.; Twele, A.; Martinis, S. Landslide mapping in vegetated areas using change detection based on optical and polarimetric sar data. *Remote Sens.* **2016**, *8*, 307. [CrossRef]

16. Raspini, F.; Ciampalini, A.; Del Conte, S.; Lombardi, L.; Nocentini, M.; Gigli, G.; Ferretti, A.; Casagli, N. Exploitation of amplitude and phase of satellite sar images for landslide mapping: The case of montescaglioso (South Italy). *Remote Sens.* **2015**, *7*, 14576–14596. [CrossRef]

17. Shi, X.; Liao, M.; Li, M.; Zhang, L.; Cunningham, C. Wide-area landslide deformation mapping with multi-path alos palsar data stacks: A case study of three gorges area, China. *Remote Sens.* **2016**, *8*, 136. [CrossRef]

18. Kawabata, D.; Bandibas, J. Landslide susceptibility mapping using geological data, a dem from aster images and an artificial neural network (ANN). *Geomorphology* **2009**, *113*, 97–109. [CrossRef]

19. Oh, H.-J.; Park, N.-W.; Lee, S.-S.; Lee, S. Extraction of landslide-related factors from aster imagery and its application to landslide susceptibility mapping. *Int. J. Remote Sens.* **2012**, *33*, 3211–3231. [CrossRef]

20. Zhao, C.; Zhong, L. Remote Sensing of Landslides—A Review. *Remote. Sens.* **2018**, *10*, 279. [CrossRef]

21. Stumpf, A.; Michéa, D.; Malet, J.P. Improved Co-Registration of Sentinel-2 and Landsat-8 Imagery for Earth Surface Motion Measurements. *Remote Sens.* **2018**, *10*, 160. [CrossRef]

22. Ercanoglu, M.; Gokceoglu, C.; Van Asch, T.W. Landslide susceptibility zoning north of yenice (NW Turkey) by multivariate statistical techniques. *Nat. Hazards* **2004**, *32*, 1–23. [CrossRef]

23. Gupta, R.; Joshi, B. Landslide hazard zoning using the gis approach—A case study from the ramganga catchment, himalayas. *Eng. Geol.* **1990**, *28*, 119–131. [CrossRef]

24. Van Westen, C. GIS in landslide hazard zonation: A review, with examples from the andes of colombia. In *Mountain Environment Regional Information Systems*; Taylor & Francis: London, UK, 1994; pp. 135–166, ISBN 0-7484-0088-5.

25. Nagarajan, R.; Mukherjee, A.; Roy, A.; Khire, M. Technical note temporal remote sensing data and GIS application in landslide hazard zonation of part of western ghat, India. *Int. J. Remote Sens.* **1998**, *19*, 573–585. [CrossRef]

26. Constantin, M.; Bednarik, M.; Jurchescu, M.C.; Vlaicu, M. Landslide susceptibility assessment using the bivariate statistical analysis and the index of entropy in the Sibiciu basin (Romania). *Environ. Earth Sci.* **2011**, *63*, 397–406. [CrossRef]

27. Blahut, J.; Klimeš, J.; Vařilová, Z. Quantitative rockfall hazard and risk analysis in selected municipalities of the české švýcarsko national park, northwestern Czechia. *Geografie* **2013**, *118*, 205–220.

28. Ciabatta, L.; Brocca, L.; Massari, C.; Moramarco, T.; Puca, S.; Rinollo, A.; Gabellani, S.; Wagner, W. Integration of satellite soil moisture and rainfall observations over the Italian territory. *J. Hydrometeorol.* **2015**, *16*, 1341–1355. [CrossRef]

29. Oliveira, S.; Zêzere, J.; Catalão, J.; Nico, G. The contribution of psinsar interferometry to landslide hazard in weak rock-dominated areas. *Landslides* **2015**, *12*, 703–719. [CrossRef]

30. Shahabi, H.; Hashim, M. Landslide susceptibility mapping using GIS-based statistical models and remote sensing data in tropical environment. *Sci. Rep.* **2015**, *5*, 9899. [CrossRef] [PubMed]

31. Tan, Y.; Guo, D.; Xu, B. A geospatial information quantity model for regional landslide risk assessment. *Nat. Hazards* **2015**, *79*, 1385–1398. [CrossRef]

32. Jebur, M.N.; Pradhan, B.; Tehrany, M.S. Using alos palsar derived high-resolution dinsar to detect slow-moving landslides in tropical forest: Cameron highlands, malaysia. *Geomat. Nat. Hazards Risk* **2015**, *6*, 741–759. [CrossRef]

33. Vahidnia, M.H.; Alesheikh, A.A.; Alimohammadi, A.; Hosseinali, F. A GIS-based neuro-fuzzy procedure for integrating knowledge and data in landslide susceptibility mapping. *Comput. Geosci.* **2010**, *36*, 1101–1114. [CrossRef]

34. Yalcin, A. GIS-based landslide susceptibility mapping using analytical hierarchy process and bivariate statistics in ardesen (Turkey): Comparisons of results and confirmations. *Catena* **2008**, *72*, 1–12. [CrossRef]

35. Mondal, S.; Maiti, R. Landslide susceptibility analysis of Shiv-khola watershed, Darjiling: A Remote sensing & GIS based analytical hierarchy process (AHP). *J. Indian Soc. Remote Sens.* **2012**, *40*, 483–496.

36. Kayastha, P.; Dhital, M.; De Smedt, F. Application of the analytical hierarchy process (AHP) for landslide susceptibility mapping: A case study from the Tinau Watershed, west Nepal. *Comput. Geosci.* **2013**, *52*, 398–408. [CrossRef]

37. Shahabi, H.; Khezri, S.; Ahmad, B.B.; Hashim, M. Landslide susceptibility mapping at central Zab basin, Iran: A comparison between analytical hierarchy process, frequency ratio and logistic regression models. *Catena* **2014**, *115*, 55–70. [CrossRef]

38. Nefeslioglu, H.; Gokceoglu, C.; Sonmez, H. An assessment on the use of logistic regression and artificial neural networks with different sampling strategies for the preparation of landslide susceptibility maps. *Eng. Geol.* **2008**, *97*, 171–191. [CrossRef]

39. Yilmaz, I. Landslide susceptibility mapping using frequency ratio, logistic regression, artificial neural networks and their comparison: A case study from Kat Landslides (Tokat—Turkey). *Comput. Geosci.* **2009**, *35*, 1125–1138. [CrossRef]

40. Pradhan, B.; Lee, S. Regional landslide susceptibility analysis using back-propagation neural network model at Cameron Highland, Malaysia. *Landslides* **2010**, *7*, 13–30. [CrossRef]

41. Akgun, A.; Kıncal, C.; Pradhan, B. Application of remote sensing data and gis for landslide risk assessment as an environmental threat to Izmir city (West Turkey). *Environ. Monit. Assess.* **2012**, *184*, 5453–5470. [CrossRef] [PubMed]

42. Wang, L.-J.; Sawada, K.; Moriguchi, S. Landslide susceptibility analysis with logistic regression model based on fcm sampling strategy. *Comput. Geosci.* **2013**, *57*, 81–92. [CrossRef]

43. Regmi, A.D.; Yoshida, K.; Pourghasemi, H.R.; DhitaL, M.R.; Pradhan, B. Landslide susceptibility mapping along Bhalubang—Shiwapur area of mid-western Nepal using frequency ratio and conditional probability models. *J. Mt. Sci.* **2014**, *11*, 1266–1285. [CrossRef]

44. Shahabi, H.; Hashim, M.; Ahmad, B.B. Remote sensing and GIS-based landslide susceptibility mapping using frequency ratio, logistic regression, and fuzzy logic methods at the central Zab basin, Iran. *Environ. Earth Sci.* **2015**, *73*, 8647–8668. [CrossRef]

45. Parise, M.; Jibson, R.W. A seismic landslide susceptibility rating of geologic units based on analysis of characteristics of landslides triggered by the 17 January, 1994 northridge, california earthquake. *Eng. Geol.* **2000**, *58*, 251–270. [CrossRef]

46. Jibson, R.W.; Harp, E.L.; Michael, J.A. A method for producing digital probabilistic seismic landslide hazard maps. *Eng. Geol.* **2000**, *58*, 271–289. [CrossRef]

47. Cevik, E.; Topal, T. GIS-based landslide susceptibility mapping for a problematic segment of the natural gas pipeline, Hendek (Turkey). *Environ. Geol.* **2003**, *44*, 949–962. [CrossRef]

48. Akgün, A.; Bulut, F. GIS-based landslide susceptibility for arsin-yomra (Trabzon, North Turkey) region. *Environ. Geol.* **2007**, *51*, 1377–1387. [CrossRef]

49. Dahal, R.K.; Hasegawa, S.; Nonomura, A.; Yamanaka, M.; Masuda, T.; Nishino, K. GIS-based weights-of-evidence modeling of rainfall-induced landslides in small catchments for landslide susceptibility mapping. *Environ. Geol.* **2008**, *54*, 311–324. [CrossRef]

50. Remondo, J.; González, A.; De Terán, J.R.D.; Cendrero, A.; Fabbri, A.; Chung, C.-J.F. Validation of landslide susceptibility maps; examples and applications from a case study in Northern Spain. *Nat. Hazards* **2003**, *30*, 437–449. [CrossRef]

51. Devkota, K.C.; Regmi, A.D.; Pourghasemi, H.R.; Yoshida, K.; Pradhan, B.; Ryu, I.C.; Dhital, M.R.; Althuwaynee, O.F. Landslide susceptibility mapping using certanty factor, index of entropy and logistic regression models in GIS and their comparison at mugling–narayanghat road section in Nepal Himalaya. *Nat. Hazards* **2013**, *65*, 135–165. [CrossRef]

52. Pourghasemi, H.R.; Pradhan, B.; Gokceoglu, C.; Mohammadi, M.; Moradi, H.R. Application of weights-of-evidence and certanty factor models and their comparison in landslide susceptibility mapping at Haraz watershed, Iran. *Arab. J. Geosci.* **2013**, *6*, 2351–2365. [CrossRef]

53. Binaghi, E.; Luzi, L.; Madella, P.; Pergalani, F.; Rampini, A. Slope instability zonation: A comparison between certanty factor and fuzzy Dempster–Shafer approaches. *Nat. Hazards* **1998**, *17*, 77–97. [CrossRef]

54. Ozdemir, A.; Altural, T. A comparative study of frequency ratio, weights of evidence and logistic regression methods for landslide susceptibility mapping: Sultan mountains, SW Turkey. *J. Asian Earth Sci.* **2013**, *64*, 180–197. [CrossRef]

55. Regmi, A.D.; Devkota, K.C.; Yoshida, K.; Pradhan, B.; Pourghasemi, H.R.; Kumamoto, T.; Akgun, A. Application of frequency ratio, statistical index, and weights-of-evidence models and their comparison in landslide susceptibility mapping in central Nepal himalaya. *Arab. J. Geosci.* **2014**, *7*, 725–742. [CrossRef]

56. Althuwaynee, O.F.; Pradhan, B.; Park, H.-J.; Lee, J.H. A novel ensemble bivariate statistical evidential belief function with knowledge-based analytical hierarchy process and multivariate statistical logistic regression for landslide susceptibility mapping. *Catena* **2014**, *114*, 21–36. [CrossRef]

57. Tien Bui, D.; Pradhan, B.; Revhaug, I.; Nguyen, D.B.; Pham, H.V.; Bui, Q.N. A novel hybrid evidential belief function-based fuzzy logic model in spatial prediction of rainfall-induced shallow landslides in the Lang Son city area (Vietnam). *Geomat. Nat. Hazards Risk* **2015**, *6*, 243–271.

58. Chen, W.; Pourghasemi, H.R.; Zhao, Z. A GIS-based comparative study of dempster-shafer, logistic regression and artificial neural network models for landslide susceptibility mapping. *Geocarto Int.* **2017**, *32*, 367–385. [CrossRef]

59. Tien Bui, D.; Pradhan, B.; Lofman, O.; Revhaug, I.; Dick, O.B. Spatial prediction of landslide hazards in HOA Binh province (Vietnam): A comparative assessment of the efficacy of evidential belief functions and fuzzy logic models. *Catena* **2012**, *96*, 28–40. [CrossRef]

60. Dou, J.; Yamagishi, H.; Pourghasemi, H.R.; Yunus, A.P.; Song, X.; Xu, Y.; Zhu, Z. An integrated artificial neural network model for the landslide susceptibility assessment of Osado Island, Japan. *Nat. Hazards* **2015**, *78*, 1749–1776. [CrossRef]

61. Polykretis, C.; Ferentinou, M.; Chalkias, C. A comparative study of landslide susceptibility mapping using landslide susceptibility index and artificial neural networks in the Krios River and Krathis River catchments (Northern Peloponnesus, Greece). *Bull. Eng. Geol. Environ.* **2015**, *74*, 27–45. [CrossRef]

62. Tien Bui, D.; Tuan, T.A.; Klempe, H.; Pradhan, B.; Revhaug, I. Spatial prediction models for shallow landslide hazards: A comparative assessment of the efficacy of support vector machines, artificial neural networks, kernel logistic regression, and logistic model tree. *Landslides* **2016**, *13*, 361–378. [CrossRef]

63. Chen, W.; Pourghasemi, H.R.; Naghibi, S.A. Prioritization of landslide conditioning factors and its spatial modeling in Shangnan county, China using GIS-based data mining algorithms. *Bull. Eng. Geol. Environ.* **2018**, *77*, 611–629. [CrossRef]

64. Chen, W.; Xie, X.; Wang, J.; Pradhan, B.; Hong, H.; Bui, D.T.; Duan, Z.; Ma, J. A comparative study of logistic model tree, random forest, and classification and regression tree models for spatial prediction of landslide susceptibility. *CATENA* **2017**, *151*, 147–160. [CrossRef]

65. Chen, W.; Peng, J.; Hong, H.; Shahabi, H.; Pradhan, B.; Liu, J.; Zhu, A.X.; Pei, X.; Duan, Z. Landslide susceptibility modeling using GIS-based machine learning techniques for Chongren County, Jiangxi Province, China. *Sci. Total Environ.* **2018**, *626*, 1121–1135. [CrossRef] [PubMed]

66. Trigila, A.; Iadanza, C.; Esposito, C.; Scarascia-Mugnozza, G. Comparison of logistic regression and random forests techniques for shallow landslide susceptibility assessment in Giampilieri (NE Sicily, Italy). *Geomorphology* **2015**, *249*, 119–136. [CrossRef]

67. Chen, W.; Xie, X.; Peng, J.; Wang, J.; Duan, Z.; Hong, H. Gis-based landslide susceptibility modeling: A comparative assessment of kernel logistic regression, naïve-bayes tree, and alternating decision tree models. *Geomat. Nat. Hazards Risk* **2017**, *8*, 950–973. [CrossRef]

68. Hong, H.; Pradhan, B.; Xu, C.; Bui, D.T. Spatial prediction of landslide hazard at the Yihuang area (China) using two-class kernel logistic regression, alternating decision tree and support vector machines. *Catena* **2015**, *133*, 266–281. [CrossRef]

69. Pradhan, B. A comparative study on the predictive ability of the decision tree, support vector machine and neuro-fuzzy models in landslide susceptibility mapping using GIS. *Comput. Geosci.* **2013**, *51*, 350–365. [CrossRef]

70. Chen, W.; Wang, J.; Xie, X.; Hong, H.; Trung, N.V.; Bui, D.T.; Wang, G.; Li, X. Spatial prediction of landslide susceptibility using integrated frequency ratio with entropy and support vector machines by different kernel functions. *Environ. Earth Sci.* **2016**, *75*, 1344. [CrossRef]

71. Hong, H.; Pradhan, B.; Jebur, M.N.; Bui, D.T.; Xu, C.; Akgun, A. Spatial prediction of landslide hazard at the Luxi area (China) using support vector machines. *Environ. Earth Sci.* **2016**, *75*, 1–14. [CrossRef]

72. Tien Bui, D.; Pham, B.T.; Nguyen, Q.P.; Hoang, N.-D. Spatial prediction of rainfall-induced shallow landslides using hybrid integration approach of least-squares support vector machines and differential evolution optimization: A case study in central Vietnam. *Int. J. Digit. Earth* **2016**, *9*, 1077–1097. [CrossRef]

73. Chen, W.; Pourghasemi, H.R.; Naghibi, S.A. A comparative study of landslide susceptibility maps produced using support vector machine with different kernel functions and entropy data mining models in China. *Bull. Eng. Geol. Environ.* **2017**, *77*, 647–664. [CrossRef]

74. Tien Bui, D.; Pradhan, B.; Lofman, O.; Revhaug, I. Landslide susceptibility assessment in Vietnam using support vector machines, decision tree, and naive bayes models. *Math. Probl. Eng.* **2012**, *2012*, 974638. [CrossRef]

75. Dehnavi, A.; Aghdam, I.N.; Pradhan, B.; Varzandeh, M.H.M. A new hybrid model using step-wise weight assessment ratio analysis (SWARA) technique and adaptive neuro-fuzzy inference system (ANFIS) for regional landslide hazard assessment in Iran. *Catena* **2015**, *135*, 122–148. [CrossRef]

76. Aghdam, I.N.; Varzandeh, M.H.M.; Pradhan, B. Landslide susceptibility mapping using an ensemble statistical index (WI) and adaptive neuro-fuzzy inference system (ANFIS) model at Alborz mountains (Iran). *Environ. Earth Sci.* **2016**, *75*, 1–20. [CrossRef]

77. Lee, S.; Ryu, J.-H.; Won, J.-S.; Park, H.-J. Determination and application of the weights for landslide susceptibility mapping using an artificial neural network. *Eng. Geol.* **2004**, *71*, 289–302. [CrossRef]

78. He, S.; Pan, P.; Dai, L.; Wang, H.; Liu, J. Application of kernel-based fisher discriminant analysis to map landslide susceptibility in the Qinggan river delta, three Gorges, China. *Geomorphology* **2012**, *171*, 30–41. [CrossRef]

79. Peng, L.; Niu, R.; Huang, B.; Wu, X.; Zhao, Y.; Ye, R. Landslide susceptibility mapping based on rough set theory and support vector machines: A case of the three Gorges area, China. *Geomorphology* **2014**, *204*, 287–301. [CrossRef]

80. Chang, S.-H.; Wan, S. Discrete rough set analysis of two different soil-behavior-induced landslides in national Shei-pa park, Taiwan. *Geosci. Front.* **2015**, *6*, 807–816. [CrossRef]

81. Metcalfe, I. Tectonic evolution of the Malay peninsula. *J. Asian Earth Sci.* **2013**, *76*, 195–213. [CrossRef]

82. Pradhan, B. Remote sensing and GIS-based landslide hazard analysis and cross-validation using multivariate logistic regression model on three test areas in Malaysia. *Adv. Space Res.* **2010**, *45*, 1244–1256. [CrossRef]

83. Qiao, G.; Lu, P.; Scaioni, M.; Xu, S.; Tong, X.; Feng, T.; Wu, H.; Chen, W.; Tian, Y.; Wang, W. Landslide investigation with remote sensing and sensor network: From susceptibility mapping and scaled-down simulation towards in situ sensor network design. *Remote Sens.* **2013**, *5*, 4319–4346. [CrossRef]

84. Varnes, D.J. Slope movement types and processes. *Spéc. Rep.* **1978**, *176*, 11–33.

85. Blaschke, T. Object based image analysis for remote sensing. *ISPRS J. Photogramm. Remote Sens.* **2010**, *65*, 2–16. [CrossRef]

86. Gibson, P.J.; Power, C.H.; Goldin, S.E.; Rudahl, K.T. *Introductory Remote Sensing: Digital Image Processing and Applications*; Routledge: London, UK, 2000; Volume 11.

87. Askne, J.; Santoro, M. Multitemporal repeat pass sar interferometry of boreal forests. *Geosci. Remote Sens. IEEE Trans.* **2005**, *43*, 1219–1228. [CrossRef]

88. Yonezawa, C.; Watanabe, M.; Saito, G. Polarimetric decomposition analysis of alos palsar observation data before and after a landslide event. *Remote Sens.* **2012**, *4*, 2314–2328. [CrossRef]

89. Oh, H.-J.; Pradhan, B. Application of a neuro-fuzzy model to landslide-susceptibility mapping for shallow landslides in a tropical hilly area. *Comput. Geosci.* **2011**, *37*, 1264–1276. [CrossRef]

90. Wan, S.; Lei, T.C. A knowledge-based decision support system to analyze the debris-flow problems at Chen-yu-lan river, Taiwan. *Knowl.-Based Syst.* **2009**, *22*, 580–588. [CrossRef]

91. Wang, Y.-N.; Yuan, X.-F. SVM approximate-based internal model control strategy. *Acta Autom. Sin.* **2008**, *34*, 172–179. [CrossRef]

92. Tehrany, M.S.; Pradhan, B.; Jebur, M.N. Flood susceptibility mapping using a novel ensemble weights-of-evidence and support vector machine models in GIS. *J. Hydrol.* **2014**, *512*, 332–343. [CrossRef]

93. Shirzadi, A.; Shahabi, H.; Chapi, K.; Bui, D.T.; Pham, B.T.; Shahedi, K.; Ahmad, B.B. A comparative study between popular statistical and machine learning methods for simulating volume of landslides. *CATENA* **2017**, *157*, 213–226. [CrossRef]

94. Xu, C.; Dai, F.; Xu, X.; Lee, Y.H. GIS-based support vector machine modeling of earthquake-triggered landslide susceptibility in the Jianjiang river watershed, China. *Geomorphology* **2012**, *145*, 70–80. [CrossRef]

95. Vapnik, V. *The Nature of Statistical Learning Theory*; Springer: Berlin, Germany, 2013.

96. Wu, X.; Ren, F.; Niu, R. Landslide susceptibility assessment using object mapping units, decision tree, and support vector machine models in the three Gorges of China. *Environ. Earth Sci.* **2014**, *71*, 4725–4738. [CrossRef]

97. Kavzoglu, T.; Colkesen, I. A kernel functions analysis for support vector machines for land cover classification. *Int. J. Appl. Earth Obs. Geoinf.* **2009**, *11*, 352–359. [CrossRef]

98. Pourghasemi, H.R.; Jirandeh, A.G.; Pradhan, B.; Xu, C.; Gokceoglu, C. Landslide susceptibility mapping using support vector machine and GIS at the Golestan province, Iran. *J. Earth Syst. Sci.* **2013**, *122*, 349–369. [CrossRef]

99. Hong, H.; Chen, W.; Xu, C.; Youssef, A.M.; Pradhan, B.; Tien Bui, D. Rainfall-induced landslide susceptibility assessment at the Chongren area (China) using frequency ratio, certainty factor, and index of entropy. *Geocarto Int.* **2017**, *32*, 139–154. [CrossRef]

100. Youssef, A.M.; Al-Kathery, M.; Pradhan, B. Landslide susceptibility mapping at Al-hasher area, Jizan (Aaudi Arabia) using GIS-based frequency ratio and index of entropy models. *Geosci. J.* **2015**, *19*, 113–134. [CrossRef]

101. Shadman Roodposhti, M.; Aryal, J.; Shahabi, H.; Safarrad, T. Fuzzy shannon entropy: A hybrid GIS-based landslide susceptibility mapping method. *Entropy* **2016**, *18*, 343. [CrossRef]

102. Bednarik, M.; Magulová, B.; Matys, M.; Marschalko, M. Landslide susceptibility assessment of the Kraľovany–liptovský Mikuláš railway case study. *Phys. Chem. Earth Parts A/B/C* **2010**, *35*, 162–171. [CrossRef]

103. Shirzadi, A.; Bui, D.T.; Pham, B.T.; Solaimani, K.; Chapi, K.; Kavian, A.; Shahabi, H.; Revhaug, I. Shallow landslide susceptibility assessment using a novel hybrid intelligence approach. *Environ. Earth Sci.* **2017**, *76*, 60. [CrossRef]

104. Bennett, N.D.; Croke, B.F.; Guariso, G.; Guillaume, J.H.; Hamilton, S.H.; Jakeman, A.J.; Marsili-Libelli, S.; Newham, L.T.; Norton, J.P.; Perrin, C. Characterising performance of environmental models. *Environ. Model. Softw.* **2013**, *40*, 1–20. [CrossRef]

105. Landis, J.R.; Koch, G.G. The measurement of observer agreement for categorical data. *Biometrics* **1977**, *33*, 159–174. [CrossRef] [PubMed]

106. Pham, B.T.; Bui, D.T.; Prakash, I.; Dholakia, M. Hybrid integration of multilayer perceptron neural networks and machine learning ensembles for landslide susceptibility assessment at himalayan area (India) using GIS. *Catena* **2017**, *149*, 52–63. [CrossRef]

107. Van Den Eeckhaut, M.; Vanwalleghem, T.; Poesen, J.; Govers, G.; Verstraeten, G.; Vandekerckhove, L. Prediction of landslide susceptibility using rare events logistic regression: A case-study in the Flemish Ardennes (Belgium). *Geomorphology* **2006**, *76*, 392–410. [CrossRef]

108. Pham, B.T.; Bui, D.T.; Prakash, I.; Dholakia, M. Rotation forest fuzzy rule-based classifier ensemble for spatial prediction of landslides using GIS. *Nat. Hazards* **2016**, *83*, 97–127. [CrossRef]

109. D'Arco, M.; Liccardo, A.; Pasquino, N. Anova-based approach for dac diagnostics. *IEEE Trans. Instrum. Meas.* **2012**, *61*, 1874–1882. [CrossRef]

110. Friedman, M. The use of ranks to avoid the assumption of normality implicit in the analysis of variance. *J. Am. Stat. Assoc.* **1937**, *32*, 675–701. [CrossRef]

111. Wilcoxon, F. Individual comparisons by ranking methods. *Biom. Bull.* **1945**, *1*, 80–83. [CrossRef]

112. Bijukchhen, S.M.; Kayastha, P.; Dhital, M.R. A comparative evaluation of heuristic and bivariate statistical modeling for landslide susceptibility mappings in Ghurmi–dhad Khola, East Nepal. *Arab. J. Geosci.* **2013**, *6*, 2727–2743. [CrossRef]

113. Gorsevski, P.V.; Brown, M.K.; Panter, K.; Onasch, C.M.; Simic, A.; Snyder, J. Landslide detection and susceptibility mapping using LiDAR and an artificial neural network approach: A case study in the Cuyahoga Valley National Park, Ohio. *Landslides* **2016**, *13*, 467–484. [CrossRef]

114. Lee, S. Landslide detection and susceptibility mapping in the Sagimakri area, Korea using KOMPSAT-1 and weight of evidence technique. *Environ. Earth Sci.* **2013**, *70*, 3197–3215. [CrossRef]

115. Cheng, G.; Guo, L.; Zhao, T.; Han, J.; Li, H.; Fang, J. Automatic landslide detection from remote-sensing imagery using a scene classification method based on BoVW and pLSA. *Int. J. Remote Sens.* **2013**, *34*, 45–59. [CrossRef]

116. Metternicht, G.; Hurni, L.; Gogu, R. Remote sensing of landslides: An analysis of the potential contribution to geo-spatial systems for hazard assessment in mountainous environments. *Remote Sens. Environ.* **2005**, *98*, 284–303. [CrossRef]

117. Ballabio, C.; Sterlacchini, S. Support vector machines for landslide susceptibility mapping: The Staffora River Basin case study, Italy. *Math. Geosci.* **2012**, *44*, 47–70. [CrossRef]

118. Marjanović, M.; Kovačević, M.; Bajat, B.; Voženílek, V. Landslide susceptibility assessment using SVM machine learning algorithm. *Eng. Geol.* **2011**, *123*, 225–234. [CrossRef]